AGU PUBLICATIONS

JGR

Journal of Geophysical Research: Atmospheres

RESEARCH ARTICLE
10.1002/2017JD027595

Special Section:
The Arctic: An AGU Joint Special Collection

Time-Dependent Cryospheric Longwave Surface Emissivity Feedback in the Community Earth System Model

Chaincy Kuo[1], Daniel R. Feldman[1], Xianglei Huang[2], Mark Flanner[2], Ping Yang[3], and Xiuhong Chen[2]

[1]Climate and Ecosystem Sciences Division, Lawrence Berkeley National Laboratory, Berkeley, CA, USA, [2]Department of Climate and Space Sciences and Engineering, University of Michigan, Ann Arbor, MI, USA, [3]Department of Atmospheric Sciences, Texas A&M University, College Station, TX, USA

Key Points:
- LW spectral surface emissivity improves CESM Arctic surface temperature bias by 6.1 ± 1.9 degrees Kelvin
- Spectral emissivity kernels computed for 200+ period are nonlinear in time
- Temporally and spatially localized atmospheric dynamics show decreased climatological seasonal sea ice emissivity radiative response in Arctic

Correspondence to:
C. Kuo,
CKuo@lbl.gov

Citation:
Kuo, C., Feldman, D. R., Huang, X., Flanner, M., Yang, P., & Chen, X. (2018). Time-dependent cryospheric longwave surface emissivity feedback in the Community Earth System Model. *Journal of Geophysical Research: Atmospheres*, *123*, 789–813. https://doi.org/10.1002/2017JD027595

Received 13 AUG 2017
Accepted 24 DEC 2017
Accepted article online 3 JAN 2018
Published online 19 JAN 2018

Abstract Frozen and unfrozen surfaces exhibit different longwave surface emissivities with different spectral characteristics, and outgoing longwave radiation and cooling rates are reduced for unfrozen scenes relative to frozen ones. Here physically realistic modeling of spectrally resolved surface emissivity throughout the coupled model components of the Community Earth System Model (CESM) is advanced, and implications for model high-latitude biases and feedbacks are evaluated. It is shown that despite a surface emissivity feedback amplitude that is, at most, a few percent of the surface albedo feedback amplitude, the inclusion of realistic, harmonized longwave, spectrally resolved emissivity information in CESM1.2.2 reduces wintertime Arctic surface temperature biases from −7.2 ± 0.9 K to −1.1 ± 1.2 K, relative to observations. The bias reduction is most pronounced in the Arctic Ocean, a region for which Coupled Model Intercomparison Project version 5 (CMIP5) models exhibit the largest mean wintertime cold bias, suggesting that persistent polar temperature biases can be lessened by including this physically based process across model components. The ice emissivity feedback of CESM1.2.2 is evaluated under a warming scenario with a kernel-based approach, and it is found that emissivity radiative kernels exhibit water vapor and cloud cover dependence, thereby varying spatially and decreasing in magnitude over the course of the scenario from secular changes in atmospheric thermodynamics and cloud patterns. Accounting for the temporally varying radiative responses can yield diagnosed feedbacks that differ in sign from those obtained from conventional climatological feedback analysis methods.

Plain Language Summary Climate models have exhibited a persistent cold-pole bias, whereby they systematically underestimate the average temperature and the amplification of climate change at high latitudes. A number of different explanations have been advanced for cold-pole biases, which can be broadly divided into radiative and dynamic explanations. Here we explore in detail a relatively novel radiative explanation for the cold-pole bias: the ice emissivity feedback. Similar to the difference in shortwave reflectivity of unfrozen and frozen surfaces, recent literature has shown that unfrozen surfaces are less emissive than frozen surfaces, which can induce a positive radiative feedback. We first present the highly nontrivial implementation of this feedback in a global circulation model (GCM) and show how to harmonize the disjointed representation of surface emissivity within the radiative transfer calculated by atmospheric and land components of a GCM. With this modified model, we show how this ice emissivity feedback depends on atmospheric water vapor and thus varies on time scales ranging from seasonal to centennial. We also show that the ice emissivity feedback is seasonally complementary to the well-known ice-albedo feedback, where the former is most influential during polar night. Finally, we show that including this feedback essentially eliminates the cold-pole bias on the model we used.

1. Introduction

The IPCC Fifth Assessment Report found that both individual models and the multimodel average surface air temperatures across the poles were significantly colder than observed (Flato et al., 2013). This bias is most pronounced in the Coupled Model Intercomparison Project-Phase 5 (CMIP5) (Taylor et al., 2012) multimodel distribution of Arctic Ocean wintertime surface air temperature (Flato et al., 2013). This points to an underestimation of high-latitude warming by current climate models, which has profound implications both for the cryosphere and for lower latitudes (Arctic Climate Impact Assessment, 2005). This problematic situation

should be rectified by identifying and fixing the sources of model error by including known physics and processes. There is growing awareness that the polar radiative energy balance is critically dependent on cloud cover and detailed cloud optical properties but that these quantities are currently poorly constrained (English et al., 2014; Gettelman et al., 2010; Kay et al., 2012). In addition, deficiencies in our understanding of the polar radiative energy balance have been identified as contributing substantially to the underestimation of polar climate change (Barton et al., 2014).

Much effort has been expended on understanding the role of ice-albedo feedback in describing these biases. Winton (2006) quantify the snow-albedo feedback in relation to other feedbacks to determine its impact on Arctic amplification but found that the snow-albedo feedback has a negligible influence. To constrain snow-albedo feedback observationally, Qu and Hall (2006) produce a model for the shortwave surface albedo kernel by developing an analytic model of the planetary albedo dependence on surface albedo. In a follow-up paper, the same authors derive physical models to describe the second factor in the snow-albedo feedback expression: the sensitivity of snow albedo to temperature change (Qu & Hall, 2007). Flanner et al. (2011) quantify the snow-albedo feedback using radiative kernels (Soden et al., 2008) and Northern Hemisphere satellite observations of albedo and surface temperature change between 1979 and 2008. In comparison to model projections of climatological feedbacks, they found that their observational estimate of the snow-albedo feedback mean was more than twice the mean value from the Coupled Model Intercomparison Project version 3 (CMIP3) models (Meehl et al., 2007). Colman (2013) applied surface albedo radiative kernel techniques to CMIP3 models and regressed ice-albedo feedbacks to explore Northern and Southern Hemisphere snow/sea ice feedback relationships across seasonal, interannual, decadal, and climatological time scales, finding statistically significant correlations between temporal scales only for Northern Hemisphere snow-albedo feedback. In a similar study contemporaneous to Colman (2013), Qu and Hall (2014) also found that Northern Hemisphere snow-albedo feedback exhibits strong correlations between seasonal and climatological scales in 25 CMIP5 models. In analyzing seasonal observational data records, Crook and Forster (2014) also found challenges in constraining climatological ice-albedo feedback when considering both the Northern and Southern Hemispheres. The average global all-sky surface albedo feedback reported in Flato et al. (2013), Colman (2013), and Qu and Hall (2014) is 0.26 ± 0.16 W/m^2/K, derived from model ensembles. A multimodel mean global clear-sky surface albedo feedback is close, 0.24 ± 0.07 W/m^2/K (Sanderson et al., 2010).

Despite the scientific focus on albedo feedbacks (Colman, 2013; Crook & Forster, 2014; Flanner et al., 2011; Qu & Hall, 2006; 2007; 2014; Winton, 2006), the model biases relative to observations are most pronounced where there is little to no solar insolation (e.g., Arctic winter), so unless indirect wintertime processes result from a poor implementation of model albedo outside of winter, other processes must be considered to explain this persistent issue. In polar regimes the radiative energy balance is also highly sensitive to longwave emission. Recent work has shown that current climate models may be missing an important "ice emissivity" feedback resulting from differential snow/ice and ocean surface emissivity in the far-infrared (FIR) wavelengths (Chen et al., 2014; Feldman et al., 2014; Huang et al., 2016). Angularly averaged emissivity (hereafter referred to simply as "emissivity") is a scaling term affecting the Planck emission of longwave radiation from materials into air, normalized by the ideal black-body emission at the same temperature. The emissivity of materials takes on values between 0 and 1, varies spectrally, and is dependent on photon dispersion relations in the longwave, as well as on the local surface radius of curvature. For example, emissivity values of frozen water in the shape of a snow grain and of an ice slab will differ. Global circulation models (GCMs) have conventionally treated emissivity as a broadband property, but such a simplification may not be appropriate given the recent theoretical updates to emissivity for a number of land surface types that show spectral dependence (Chen et al., 2014; Feldman et al., 2014; Huang et al., 2016).

Feldman et al. (2014) discussed the potential for a positive feedback whereby lower far-infrared surface emissivity values for ocean being smaller than sea ice would lead to reduced cooling in the high latitudes as sea ice loss increases with climate change. The outgoing longwave radiation flux in high-latitude and high-altitude regions is particularly sensitive to spectral surface emissivity changes as the drier atmosphere in these regions is more transparent to far-infrared surface emission than in low- to mid-latitude atmospheres, which have relatively higher total precipitable water. Therefore, correcting the representation of radiative cooling over those regions with low precipitable water so that they exhibit a realistic characterization of surface emissivity in the models is especially important. Chen et al. (2014) modeled far-infrared interactions between the surface and clouds, where the surface was assigned with snow surface spectral emissivity and ice cloud scattering was

taken into account. In that study, the net upward far-infrared flux at the surface and top of the atmosphere are both reduced for a high-latitude and altitude region where cloud top heights are 2–5 km above the surface.

These two aforementioned studies led to the development of a spectral surface emissivity database for weather and climate models, for which spectral emissivity is modeled for a number of surface types in the longwave from wavenumbers 0 to 2,000 cm^{-1} in Huang et al. (2016); complex indices of refraction of water and ice compiled for wavelengths spanning the near ultraviolet to far infrared (Hale & Querry, 1973; Warren & Brandt, 2008) are model inputs. Undisturbed water and ice emissivities are modeled with Fresnel equations on a semi-infinite half-space and snow emissivities are derived by approximating snow grains as spheres, where emissivity is equal to the absorption efficiency calculated from Mie theory with optical properties adjusted to account for diffracted electromagnetic wave coherence effects when deposited snow grains are closely packed (Mishchenko, 1994). Spectral emissivity is dependent not only on complex indices of refraction but on local curvature radii of longwave photon exittance as well, so spectral emissivity will evolve with snow grain size. Additionally, snow grain size-dependent spectral emissivities have been reported by Hori et al. (2006) and Chen et al. (2014). Due to detector material cutoff responsivity, measurements of surface emissivity exist only for wavenumbers higher than 650 cm^{-1} ($\lambda < 15.4$ μm) (Baldridge et al., 2009; Hori et al., 2006), and Huang et al. (2016) show that modeled spectral emissivity curves compare well in this range, giving confidence to the computed emissivity values extending out to the far-infrared (wavenumbers < 650 cm^{-1}).

This emissivity database can be used as part of GCM longwave radiation routines. Building on this database, Huang et al. (2016) explored global and regional differences between radiant energy fields in off-line simulations of the atmospheric component of the Community Earth System Model (Hurrell et al., 2013) with and without realistic surface emissivity. Huang et al. (2016) found that the global root-mean-square (RMS) difference in outgoing longwave radiation (OLR) between the two simulations can be as large as 2.04 W/m^2 in a summer month under clear-sky conditions.

However, to date, the effects of realistic, spectrally resolved longwave surface emissivity on a transiently forced, fully coupled climate model have not been considered, so we can compare and contrast the results from including realistic surface emissivity in a model to the heretofore conventional model treatment of surface emissivity. In this paper, we will present the detailed modifications to CESM that we used to harmonize the treatment of non-unit, spectrally resolved emissivity across all relevant model components, and then we will present an analysis of how the inclusion of realistic surface emissivity affects model polar biases. Finally, we present appropriate, computationally efficient methods for diagnosing a GCM's ice emissivity feedbacks and their temporal and spatial dependence, and discuss implications for the inclusion of realistic surface spectral emissivity modifications for other widely used climate models besides CESM.

2. Methods

2.1. Emissivity Specification in CESM

In the release version of CESM1, the surface components of that code calculate the grey-body broadband longwave upwelling surface flux using broadband emissivity values ϵ. Specifically in the land component, grey-body broadband longwave upwelling surface flux $F^{\uparrow}_{surf} = \epsilon\sigma_{SB}T^4_{ground}$, where σ_{SB} is the Stefan-Boltzmann constant, and T_{ground} is the ground temperature. This longwave upwelling flux is passed from the surface components into the atmospheric component, where surface emissivity contribution to the flux is retained. To preserve this contribution, CESM1 adopts a convention whereby the surface flux in the atmospheric component at the surface boundary grid, ($F^{\uparrow}_{surf}$), is given by σT^4_{rad}, but T_{rad} is rederived by defining the radiative surface temperature of the model's surface components as follows: $T_{rad} = \sqrt[4]{F^{\uparrow}_{surf}/(\epsilon\sigma_{SB})}$, where surface emissivity is simplified to $\epsilon = 1.0$. The recalculated radiative surface temperature, distinct from the surface temperature that other model components utilize, is used in the atmospheric component as a new temperature boundary condition for longwave flux calculations by way of the Planck function integrated over all wavelengths and angles. Consequently, calculation of upward radiative fluxes in the CESM1 release version atmospheric component amounts to a Planck curve spectral modulation of the grey-body longwave upwelling radiation of the surface components.

Longwave radiative fluxes are modeled by RRTMG_LW (Mlawer et al., 1997), a rapid radiative transfer model for use in global circulation models. RRTMG_LW uses a correlated-k method with a reduced k-distribution set to calculate fluxes in global circulation models that is at least 4 orders of magnitude more computationally

Table 1
RRTMG_LW Bands (Iacono et al., 2000) and Surface Emissivity Values

RRTMG_LW		Emissivity		
Band	Limits (cm^{-1})	Snow	Ocean	Desert
1	10–350	0.9936	0.8488	0.9116
2	350–500	0.9883	0.8845	0.8866
3	500–630	0.9799	0.8874	0.9055
4	630–700	0.9717	0.899	0.9591
5	700–820	0.9643	0.9189	0.9605
6	820–980	0.982	0.9531	0.9376
7	980–1080	0.9862	0.9502	0.8783
8	1080–1180	0.9909	0.9447	0.9181
9	1180–1390	0.9812	0.9400	0.9780
10	1390–1480	0.9776	0.9362	0.9741
11	1480–1800	0.9771	0.9359	0.9705
12	1800–2080	0.9717	0.9374	0.9676
13	2080–2250	0.965	0.9349	0.9648
14	2250–2380	0.9636	0.9336	0.9648
15	2380–2600	0.9583	0.9316	0.9636
16	2600–3250	0.9391	0.9251	0.9613
Planck-averaged broadband		0.982	0.901	0.922
CESM1 broadband		0.970	1.000	0.960

efficient than line-by-line methods. The longwave spectrum is discretized into 16 contiguous bands that balance radiometric accuracy with computational efficiency, and Table 1 lists the 16 discrete, contiguous spectral bands that the atmospheric component maintains for intra-atmosphere radiative transfer.

2.2. Harmonizing Emissivity Across Model Components

In this work, we modify CESM1 to establish a coherent and energy-conserving treatment of surface emissivity between all of the surface and atmospheric components of the model. While we use the spectral emissivity values described by Feldman et al. (2014) in both the atmospheric and surface interactions in CESM, the modifications we present here supersede those of Feldman et al. (2014), which explored the sensitivity of model prognostics to only emissivity modifications to the atmospheric component of CESM. We detail the steps to harmonize longwave upwelling flux between the surface and atmospheric components below.

Selecting the medium-grained snow size emissivity curve and desert scene emissivity curve from Huang et al. (2016), we set the Planck function-weighted broadband emissivity for frozen surfaces (sea and land ice) over a T_s range 250–273 K to the average value 0.982 (deviation $\pm$0.0002), the corresponding value for nonvegetated mineralized land over T_s range 260–300 K is 0.926 (deviation $\pm$0.001), and for ocean over T_s range 253–293 K is 0.908 (deviation $\pm$0.001). The simulated spectral surface emissivity curves, Planck function-weighted broadband, and original CESM1 broadband surface emissivity values are listed in Table 1. Theoretical predictions of longwave spectral emissivity beyond 15 μm for vegetation have not been undertaken at the time of this study due to the lack of coherent measurements and/or modeling of plant pigment indices of refraction, leaf cell sizes and shapes both in its interior and epidermis, and the leaf macroscopic shape. Consequently, vegetation emissivity is left unaltered from the release version of CESM1, which is dependent on exposed leaf and stem area indices. Calculated in the land model, upwelling longwave fluxes emitted above the canopy in vegetated grid cells are preserved in the atmospheric model grid cells. Vegetated grid cells are identified in a binary fashion, on the condition where the sum of leaf area and stem area indices is >0.05. Medium-grained snow spectral emissivity is chosen for frozen surfaces, on both land and sea ice, inasmuch as sea ice is only observed to be snow-free about one month per year (Massom et al., 2001; Warren et al., 1999; Webster et al., 2014).

In the release version of CESM1, the upward longwave surface flux is preserved in the atmospheric component (Community Atmosphere Model, version 5.3) by solving for surface radiative temperature as described above.

While $\epsilon < 1.0$ in the land and ice component in the release version of CESM1, ϵ is set to unity ($\epsilon = 1.0$) in the atmospheric component, so any changes to the treatment of surface emissivity in the surface components of the model requires the rederivation of surface temperatures in the atmospheric component to avoid a mismatch, and a lack of energy conservation, between the radiative temperature used in the atmospheric and land, ocean, and ice components of the model. However, surface temperatures in the land, ocean, and ice components are established from temperature models of subsurface-layered media, therefore, the surface temperature rederivation in the CESM1 release atmospheric model by applying the Stefan-Boltzmann law on longwave surface upwelling flux with surface emissivity set equal to 1.0 constitutes a distinctly different representation of surface temperature from subsurface-layered temperature models.

To rectify the mismatch between atmospheric and surface model component treatments of upwelling longwave radiation, we modify CESM1 such that we pass the nonradiative surface temperature calculated in the surface components to the atmospheric component via the coupler. Radiative surface fluxes ($F^{\uparrow}_{\text{surf}}$) are determined with the updated broadband Planck-weighted emissivity in surface components in CESM1 and are merged onto the atmospheric grid in the coupler before being passed to the atmospheric component. We perform this Planck weighting using three-point Gauss-Legendre quadrature (Li, 2000).

In our modified version of CESM1, the atmospheric component radiative temperature is set to the ground temperature reported by the land component for nonvegetated surfaces. Over ocean scenes, the sea surface temperature from the ocean component is passed to the atmospheric component, and the atmospheric component receives proportionately weighted ground and sea surface temperatures for grid cells with partial land fraction. The longwave upward flux in vegetated grid cells takes into account longwave flux reflections between the canopy and ground. As such, the ground temperature in vegetated grid cells would not represent an appropriate lower boundary condition in the atmospheric model, as canopy reflections are not considered in the atmospheric model. Therefore, for grid cells of land/ocean overlap and vegetated surfaces, the radiative temperature in the atmospheric component is determined by $T_{\text{rad}} = \sqrt[4]{F^{\uparrow}/\sigma_{\text{SB}}}$ to preserve the upward flux determined in the surface module.

In summary, we establish the effects of the updated spectral variations in surface emissivity in model surface components that currently only support grey-body surface emissivity by creating broadband surface emissivity values through Planck function weighting. In the atmospheric component, which does support spectrally varying surface emissivity, the surface upward longwave fluxes calculated in the surface components persist by setting the surface radiative temperature to the ground temperature from the land component and the sea surface temperature from the ocean component, after which RRTMG_LW calculates upwelling band-by-band fluxes with spectrally resolved emissivity based on the scene. Discrepancies in longwave surface upwelling fluxes emanating from the different expressions between the land and atmospheric components will be quantified to legitimize the approximation.

2.3. Emissivity Radiative Response and Feedback

2.3.1. Emissivity Kernels

Using our modified version of CESM1 to account for surface emissivity variations across model components realistically, we can then investigate, diagnose, and quantify the ice emissivity feedbacks rigorously and compare them against other widely reported feedback estimates of surface albedo. We can quantify the ice emissivity feedback using a time-dependent radiative kernel method, whereby the temporal evolution of both the kernel and emissivity can be evaluated. The radiative kernel is an analytic expression of the partial derivative of the outgoing longwave radiation at the top of the atmosphere, taking into account its dependence on surface emissivity. The kernel can be calculated online during the integration of a global circulation model and accounts for changes in water vapor and cloud cover.

The derivation of the kernel is as follows: the sensitivity of the outgoing longwave radiation to changes in surface emissivity is quantified by the partial derivative of broadband outgoing longwave radiation (OLR) with respect to surface emissivity, and is given by

$$\frac{\partial \text{OLR}}{\partial \epsilon}(\vec{r},t) = \int_0^{\infty} [B(\nu,\vec{r},T_s(\vec{r},t)) - F^{\downarrow}(\nu,\vec{r},t)]\Theta(\nu,\vec{r},t)\mathrm{d}\nu \tag{1}$$

where ϵ is emissivity, time t, and for latitude ϕ and longitude θ grid box location $\vec{r} = [\phi,\theta]$. $B(\nu,\vec{r},T_s(\vec{r},t))$ is the black-body function for surface temperature $T_s(\vec{r},t)$, $F^{\downarrow}(\nu,\vec{r},t)$ is the spectral downwelling flux from the

atmosphere above the surface, and $\Theta(\nu, \vec{r}, t)$ is the flux transmittance from the surface to the top of the model. The sign convention for the emissivity kernel is positive for outgoing flux. $\Theta(\nu, \vec{r}, t)$ is dependent on the atmospheric state which is expected to evolve over CO_2 forcing periods and includes effects of water vapor and temperature profile. The emissivity kernel can be explicitly calculated within RRTMG_LW by taking advantage of calls to its subroutines. As such, the temporal emissivity kernels for both clear-sky and all-sky can be calculated online along with CESM model runs, for each grid box and time point. The kernels broken down into its spectral components $\left[\frac{\partial \mathrm{OLR}}{\partial \epsilon}\right]_i(\vec{r}, t)$ are given by equation (1) with the integration limits ν_i and ν_{i+1}, the lower and upper wavenumber band limits of RRTMG_LW band i (1).

We can use online analytical radiative kernel feedback methods similar to the numerically derived, off-line radiative feedback kernel methods by Soden et al. (2008) and Shell et al. (2008), who use 3-hourly atmospheric state outputs over one model year to derive monthly averaged four-dimensional (latitude, longitude, atmospheric level, and time) kernels for water vapor and lapse rate, and three-dimensional (latitude, longitude, and time) surface albedo kernels using a base atmosphere from a selection of global circulation models (GCM). Soden et al. (2008) and Shell et al. (2008) produced these kernels for only one model year and applied the same kernels to monthly averaged parameter perturbations derived over two time periods: 2000–2010 and 2100–2110, in a large number of GCMs for model feedback intercomparison. In this work, surface emissivity kernels are calculated for each atmospheric model time step (hourly) throughout the model run period (1850–2100), but output as monthly averages for each surface grid cell. Kernel evolution as a function of time and the linear convention proposed by Soden et al. (2008), Shell et al. (2008), and Armour et al. (2013) can be evaluated.

However, the impact of non-unit surface emissivity, and changes thereof due to evolving states of the cryosphere, is strongly dependent on column-integrated atmospheric water vapor (Feldman et al., 2014), and to account for this, surface emissivity kernels are calculated hourly for integrations spanning 1850–2100 and various emissions scenarios. We then use this information to produce monthly averaged kernels for each grid box over the entire integration period, and we can use this detailed kernel calculation to evaluate kernel evolution as a function of time and test the linear convention proposed by Soden et al. (2008), Shell et al. (2008), and Armour et al. (2013).

2.3.2. Emissivity Kernels and Radiative Response

The outgoing longwave radiation perturbation ($\delta \mathrm{OLR}_\epsilon$) due to an emissivity perturbation $\delta\epsilon$ is the product of the kernel and $\delta\epsilon$, giving an emissivity radiative response ($\mathrm{EmR}(\vec{r}, t)$):

$$\begin{aligned}\mathrm{EmR}(\vec{r}, t) &= -\delta \mathrm{OLR}_\epsilon \\ &= -\frac{1}{A(R)} \int_R \sum_{i=1}^{16} \left[\frac{\partial \mathrm{OLR}}{\partial \epsilon}\right]_i (\vec{r}, t) \delta\epsilon_i(\vec{r}, t) \mathrm{d}A(r)\end{aligned} \tag{2}$$

where i is spectral emissivity in band i, in location $\vec{r}$ at time t and t_0, for $t > t_0$, and $A(r)$ is the area at location $\vec{r}$ in the region R. The $\delta\epsilon_i(\vec{r}, t) = [\epsilon_i(\vec{r}, t) - \epsilon_i(\vec{r}, t_0)]$ for an emissivity change in band i between time t and t_0. We adopt the sign convention in such a way that emissivity radiative response is positive for a negative change in emissivity whereby outgoing radiation is reduced at time t from a reference value at time t_0, for $t > t_0$. That is, the induced radiative response due to emissivity change is positive for net incoming radiation.

2.3.3. Conventional Climatological Emissivity Feedback

Following Wetherald and Manabe (1988), we can use conventional methods to quantify the feedback associated with changing surface emissivity, λ_ϵ, by looking at the top-of-model longwave radiative perturbation induced by radiative forcing. This is given by the following expression:

$$\lambda_\epsilon = -\frac{1}{A(R)} \int_R \sum_{i=1}^{16} \left[\frac{\partial \mathrm{OLR}}{\partial \epsilon}\right]_i (\vec{r}, t) \frac{\delta\epsilon_i(\vec{r}, t)}{\delta \bar{T}_s(t)} \mathrm{d}A(r) \tag{3}$$

$$= -\frac{\delta \mathrm{OLR}_\epsilon(\vec{r}, t)}{\delta \bar{T}_s(t)} \tag{4}$$

where $\delta \bar{T}_s(t) = \bar{T}_s(t) - \bar{T}_s(t_0)$ is the global mean surface temperature change at time t, with respect to a reference climate model global mean surface temperature at time t_0. The emissivity feedback component is the emissivity radiative response normalized by the global mean temperature change, and it therefore readily fits within the context of well-established climate feedback analyses.

Based on the forward partial radiative perturbation (PRP) technique (Wetherald & Manabe, 1988), Soden et al. (2008) describe their radiative kernel technique as similar to the two-sided PRP technique (Colman & McAvaney, 1997), but the kernel technique explicitly isolates the climate variable of interest. Soden et al. (2008) showed that climate variable feedbacks are the product of kernels calculated from a reference climate state and climate variable perturbations occurring potentially decades later. Accordingly, the Soden et al. (2008) kernels are derived from a reference climate at time period t_0, so the emissivity feedback from equation (3) is dependent on $\left[\frac{\partial \mathrm{OLR}}{\partial \epsilon}\right]_i (\vec{r}, t_0)$ and $\delta\epsilon_i(\vec{r}, t) = \epsilon_i(r, t) - \epsilon_i(r, t_0)$. The validity of this approach requires stationarity in $\left[\frac{\partial \mathrm{OLR}}{\partial \epsilon}\right]_i (\vec{r}, t_0)$ over the period over which the feedback analysis is performed, which is typically multiple decades.

Under forced climate change scenarios, the atmospheric state and therefore $\left[\frac{\partial \mathrm{OLR}}{\partial \epsilon}\right]_i (\vec{r}, t)$ at time t, can be expected to evolve away from $\left[\frac{\partial \mathrm{OLR}}{\partial \epsilon}\right]_i (\vec{r}, t_0)$, because water vapor loading in the atmosphere follows thermodynamic constraints which modulate the strength of the emissivity feedback. Therefore, equation (3) is a function of the climate state and should be time dependent, such that λ_ϵ depends on the kernel from the future forced atmosphere $\left[\frac{\partial \mathrm{OLR}}{\partial \epsilon}\right]_i (\vec{r}, t)$. The emissivity kernel, and in turn, the amplitude of the associated feedback, are dependent on the kernel base state. Thus, we can evaluate temporal ice emissivity kernels and feedback estimates using a conventional climate model feedback analysis framework for a forcing climate model run to test the stationarity assumption.

Accordingly, the surface emissivity change over a multidecadal climatic model run between t and t_0 shall be noted as $\Delta\epsilon$ rather than $\delta\epsilon$ in equations (2) and (3). We determine $\Delta\epsilon_i$ in spectral band i for each grid box, year y and month m in time period t by differencing ϵ_i from the value reported over the same month and grid box over a 10 year average in the reference period t_0

$$\Delta\epsilon_i(\vec{r}, t(m, y)) = \epsilon_i(\vec{r}, t(m, y)) - \frac{1}{10}\sum_{y=1}^{10} \epsilon_i(\vec{r}, t_0(m, y)) \tag{5}$$

2.3.4. Time Dependence of Emissivity Kernels

While Soden et al. (2008) showed that one year's worth of kernel are adequate for multimodel ensemble feedback intercomparisons, they note that multiyear kernels could elucidate local feedback strengths, but multiyear numerical four-dimensional kernels are computationally expensive for multiple climate variables. However, since our surface emissivity kernel calculation has an analytic form, we can calculate these kernels online as part of the model runs to explicitly investigate regional atmospheric dynamics in the model over longer time periods (decades) than were explored previously. As part of our analysis, we can therefore capture the outgoing longwave radiation perturbation at the top of the atmosphere due to surface emissivity changes, and the evolution of these effects over decadal climatological periods, as suggested by Armour et al. (2013).

In section 2.3.3, the product of a time-dependent kernel with emissivity response and surface temperature occurring over a several decadal period intermixes the instantaneous atmospheric state used for kernel calculation with the climatological change in emissivity and surface temperature. In an analysis scheme put forth by Armour et al. (2013), if the atmospheric state is known at each time step and grid box, then an instantaneous emissivity radiative response is considered as the product of the time-dependent kernel with a synchronous emissivity response. Adjustments to longwave radiation due exclusively to emissivity changes from seasonal cryospheric melt and freeze cycles can be directly inferred from equation (2), with t in units of months and t_0 referring to the month preceding t, so that for spectral band i, $\delta\epsilon_i$ is explicitly

$$\begin{aligned}\delta\epsilon_i(\vec{r}, t(m, y)) &= \epsilon_i(\vec{r}, t) - \epsilon_i(\vec{r}, t_0) \\ &= \epsilon_i(\vec{r}, t(m, y)) - \epsilon_i(\vec{r}, t(m-1, y)).\end{aligned} \tag{6}$$

for month m in year y. Inserting equation (6) into equation (2) then gives the instantaneous monthly outgoing longwave radiative emissivity response. The relative roles of the atmosphere and surface in controlling outgoing longwave radiation can be elucidated by differences in instantaneous monthly outgoing longwave radiative emissivity response between climatological eras separated by decades.

2.4. CESM Run Configuration

For this investigation, we use a fully coupled CESM version 1 with Community Atmospheric Model version 5 with a nominal $2^\circ \times 2^\circ$ horizontal grid and the default time steps for each model component. To test the new

emissivity values implemented in the surface and atmospheric components, we created a control run with CESM1 run under unforced conditions whereby the CO_2 concentration is set to its nominal value circa 1850, and other anthropogenic greenhouse gases and aerosols remain fixed at their respective preindustrial levels. The model is started at 1850 and runs for 155 years. Initially, the model's top of the atmosphere net energy imbalance (net shortwave-net longwave flux) remained steady over a multidecadal run at approximately 1.2 W/m^2. To reduce the net radiative imbalance to within 0.5–1.0 W/m^2 so as to be consistent with estimates of the Earth's actual radiative imbalance (Hansen et al., 2005; Trenberth et al., 2009), we decreased the threshold for relative humidity for low stable clouds (CESM namelist variable `cldfrc_rhminl`) from the default value of 0.8875 to 0.8750. From this, the net radiative imbalance stabilized at 0.7 ± 0.4 W/m^2 over the 155 year run period, after a spin-up time of 10 years. This model-tuning adjustment was consistent with published approaches presented by Mauritsen et al. (2012) to reduce net radiative balance, and the tuning followed well-established tuning parameter estimation methods (Jackson et al., 2008). We call this model "1850CNTL."

With interest in model transient sensitivity relevance to the Earth's present climate (Winton, 2006), we also ran a forced simulation with historical CO_2 concentrations, where atmospheric CO_2 concentrations from 1850 to 1950 were scaled by the ratio of the concentration derived from Siple Station ice core data in a given year to its concentration in 1850 (Neftel et al., 1994). Atmospheric CO_2 between 1976 and 2005 was set by the annually averaged Mauna Loa Observatory data (NOAA ESRL Global Monitoring Division, 2015), and atmospheric CO_2 between 1951 and 1975 was derived from a linear interpolation of the Siple Station and Mauna Loa datasets. Accordingly, the rate of increase of atmospheric CO_2 from 1850 to 1950 is approximately 0.09% per year, and from 1951 to 1974, it is approximately 0.24% per year, and from 1975 to 2005, it is approximately 0.50% per year. The threshold for relative humidity for low stable clouds was set equal to the value specified for the control case. The historical CO_2 ramping case was run for 155 years as well for the time period 1850–2005. This model will be named "HISTCO2."

In two additional cases, atmospheres defined by representative concentration pathways defined by the Intergovernmental Panel on Climate Change (IPCC) were initiated to evaluate the effect of surface emissivity on the 21st century climate. Again, the threshold for relative humidity for low stable clouds was set equal to the value specified for the 1850CNTL case. We use the CESM1 fully coupled component sets and the RCP 2.6 and RCP 8.5 forcings pathways, and start the runs referencing the 2005 HISTCO2 model and integrate to 2100. These cases are simply named "RCP2.6" and "RCP8.5."

2.5. CESM Output Data

CESM model data values were averaged monthly for subsequent analysis. The `radlw.f90` and `radiation.f90` codes were modified to output clear-sky and all-sky spectral emissivity kernels, as well as the modified spectral emissivity values on the atmospheric horizontal grid. Monthly averaged spectral emissivity kernel and emissivity maps in each of the 16 bands were written to the CESM history files.

3. Results

3.1. Model Validation

The modifications to the longwave physical representations in the model that are described above can potentially destabilize the model's climate simulations, given the specific tunings of the release version. For 1850CNTL, we evaluated the stability of climatic model variables. Over the 155 year period, the net radiative imbalance was reported above at +0.7 ± 0.4 W/m^2, the mean surface temperature was 287.12 ± 0.11 K with a rate of change of $+1.6 \pm 2.1 \times 10^{-4}$ K/yr. The sea surface temperature mean was 285.71 ± 0.06 K with a rate of change of $+0.9 \pm 1.1 \times 10^{-4}$ K/yr. Flux differences between model components are expected given that surfaces fluxes are calculated in the land model using the Stefan-Boltzmann law along with Planck-averaged emissivity, and surface fluxes in the atmospheric model are computed with an integration of Planck function using spectral emissivities. Inspection of the mean globally averaged longwave upwelling surface flux difference between the atmospheric model and land model is $1.3 \pm 0.1 \times 10^{-2}$ W/m^2, with a $-5.3 \pm 19.1 \times 10^{-6}$ W/m^2/yr rate of change over the 155 year model run.

Additionally, to benchmark our 1850 control climate against the CESM standard release, we compared the surface temperature evolution of 1850CNTL against the fully coupled 1850 control run from the CESM Last Millenium Ensemble (CESM-LME, Otto-Bliesner et al., 2016), which uses the same code version (CESM1 with CAM5.3) as the CESM Large Ensemble (CESM-LENS, Kay et al., 2015), except that CESM-LME is specified

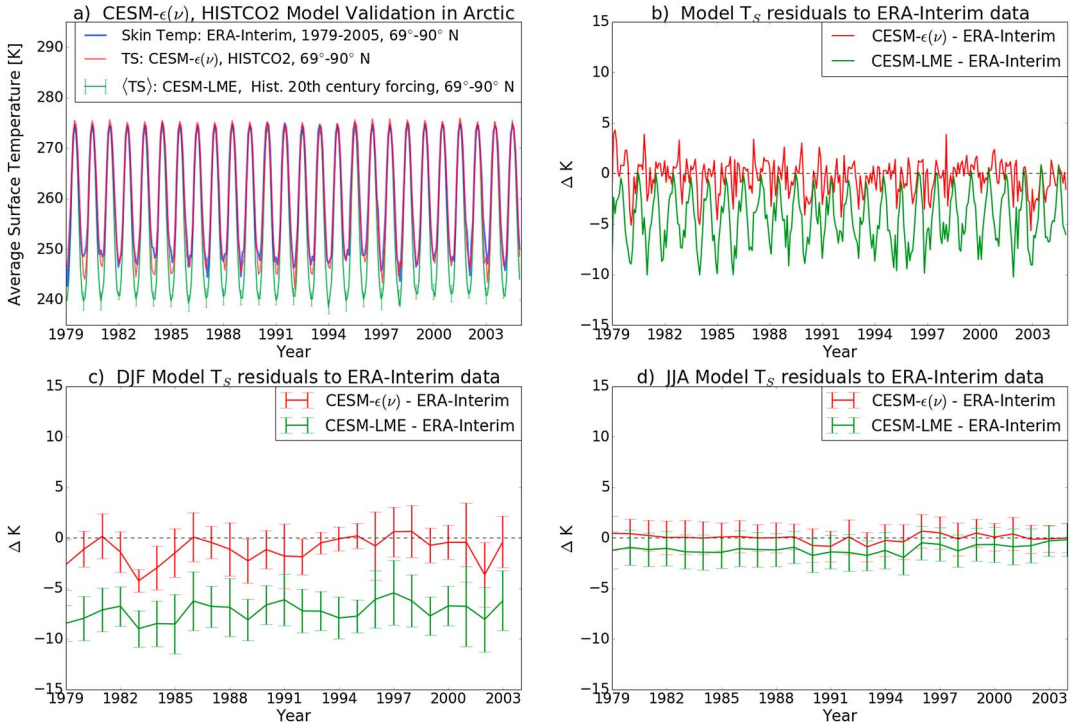

Figure 1. Focusing on Arctic Ocean latitudes, (a) comparison of 1979–2005 Arctic surface temperatures monthly and spatially averaged over 69°–90°N for CESM-$\epsilon(\nu)$ (red), the mean of 10 fully forced CESM-LME models (green), and ERA-Interim skin temperature reanalysis (blue); (b) the residuals with respect to ERA-Interim skin temperature for CESM -$\epsilon(\nu)$ radiative surface temperature (red) and CESM-LME (green); (c) December-January-February residuals for the same period and region where error bars show the deviations over the months; and (d) the June-July-August residuals for the same period and region.

on a 2° horizontal resolution grid for the atmosphere and land surface rather than the 1° for CESM-LENS. Mean surface temperature, deviation, and temperature rate of change over 1850–2005 are [287.12 ± 0.11 K, $+1.6 \times 10^{-4}$ K/yr] and [287.16 ± 0.43 K, $+1.18 \times 10^{-4}$ K/yr] for our 1850 control model and the CESM-LME 1850 fully coupled control model, respectively. The mean temperature difference of 0.04 K is within 10% of the temperature spread of 0.4 K due to internal variability in the CESM-LME member. The differences in these results are not statistically significant, so we can say that our realistic surface emissivity modifications to CESM1 do not appreciably affect unforced simulations.

3.1.1. Observational Validation

We are interested in confronting the results of our modified and unmodified versions of CESM with observations. The spectral surface emissivity-treated model, designated "CESM-$\epsilon(\nu)$," is tested against the CESM-LME (Otto-Bliesner et al., 2016), for agreement with historical (1979–2005) Arctic surface temperatures, as determined from ERA-Interim (Dee et al., 2011) skin temperature reanalysis.

Figure 1a shows a comparison of ERA-Interim skin temperatures in blue, HISTCO2 case of CESM-$\epsilon(\nu)$ in red, and CESM-LME in green over northern ocean latitudes from 1979 to 2005. Over the 26 year period, the mean temporally and spatially averaged surface temperature bias for CESM-$\epsilon(\nu)$ improves over the twentieth historical forcing CESM-LME model by over 90%, from −4.4 ± 2.7 K CESM-LME mean surface temperature bias to −0.4 ± 1.6 K CESM-$\epsilon(\nu)$ mean surface temperature bias with respect to reanalysis data, as seen in the Figure 1b residual plots. Reanalysis skin temperatures exhibit warmer mean Arctic surface temperatures than the models during the wintertime with a larger winter cold bias in the CESM-LME twentieth century model than CESM-$\epsilon(\nu)$ ($\Delta T_S^{\mathrm{LME}} = -7.2 \pm 0.9$ K versus $\Delta T_S^{\epsilon(\nu)} = -1.1 \pm 1.2$ K in Figure 1c). Summertime model surface temperature biases to skin temperature reanalysis are $\Delta T_S^{\mathrm{LME}} = -1.1 \pm 0.4$ K and $\Delta T_S^{\epsilon(\nu)} = 0.0 \pm 0.4$ K, shown in Figure 1d.

Mean Arctic surface temperature residuals are mapped for winter (Figures 2a and 2b), and summer months (Figures 2d and 2e) over 1979–2005, where the CESM-LME surface temperature winter cold bias with respect

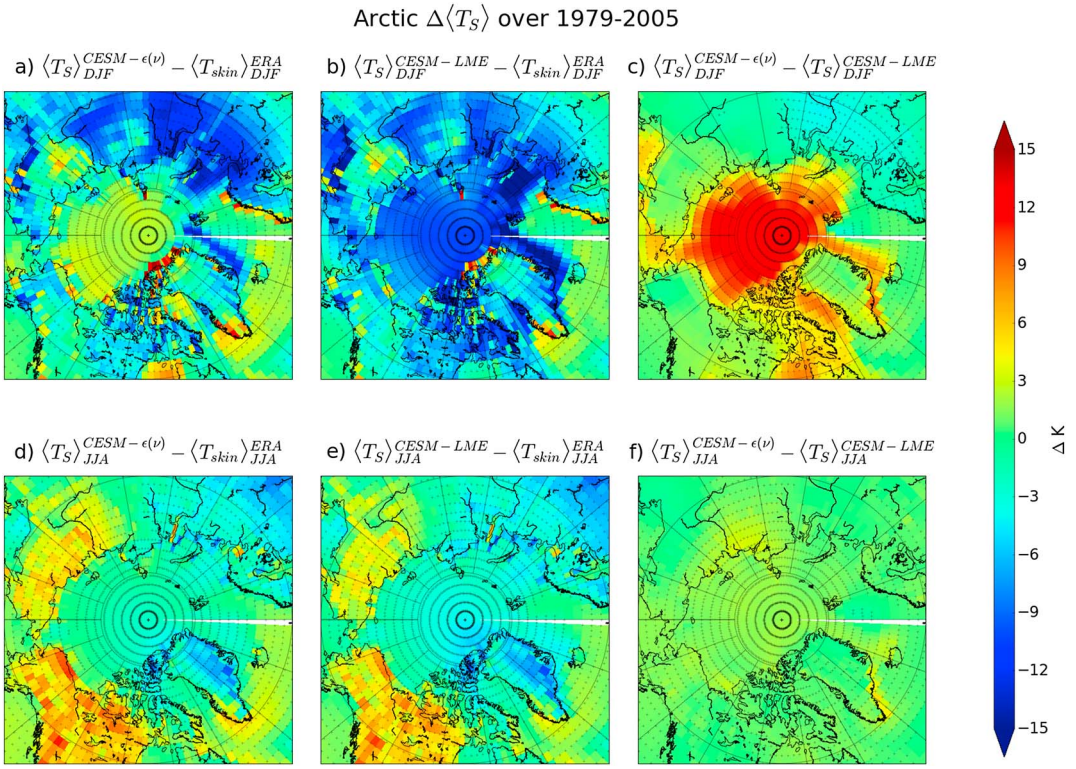

Figure 2. North Pole projection difference maps of Arctic radiative surface temperatures in the period 1979–2005 over 60°–90° northern latitudes. Skin temperature reanalysis data are from ERA-Interim (Dee et al., 2011), CESM-LME is the 10 ensemble mean of historical twentieth century fully forced model from the CESM Last Millenium Ensemble (Otto-Bliesner et al., 2016), and CESM-$\epsilon(\nu)$ is this work's model, for the HISTCO2 case. December-January-February (DJF) mean surface temperature differences are plotted between (a) CESM-$\epsilon(\nu)$ and ERA-Interim, (b) CESM-LME and ERA-Interim; and (c) CESM-$\epsilon(\nu)$-CESM-LME. (d–f) The same for months June-July-August (JJA). Crosses indicate statistically significant grid points to $p < 0.05$ of the Welch's t test.

to reanalysis data is most pronounced (Figure 2b). In Figure 2c, modeled surface temperature difference maps show that CESM-$\epsilon(\nu)$ December-January-February mean over 1979–2005 Arctic ocean surface temperature is warmer than that of CESM-LME over areas of sea ice. The cold bias pattern seen over northern Eurasia in CESM-LME (Figure 2b), associated with snow cover bias in CESM1 (Park et al., 2014), persists in CESM-$\epsilon(\nu)$ (Figure 2a). Surface temperature over land is largely unchanged between CESM-$\epsilon(\nu)$ and CESM-LME because longwave surface upwelling radiation modeling over vegetated land grids in CESM-LME remained intact in CESM-$\epsilon(\nu)$, as discussed in section 2.2. The CESM-$\epsilon(\nu)$ Arctic sea ice decline is -5.9 ± 1.2%/decade over 1950–2005, while 10 member mean CESM-LME September sea ice decline is -2.5 ± 0.4%/decade over the same period, from 60° to 90°N; we note that the uncertainty in CESM-$\epsilon(\nu)$'s sea ice decline is much larger, being a single model realization. Indeed, Stroeve et al. (2007) determined a September Arctic sea ice decline of -7.8 ± 0.6%/decade over 1953–2006 observational record, whereas the multimodel IPCC AR4 mean is -2.5 ± 0.2%/decade. Improvement of Arctic sea ice trend estimates relative to observations suggests that preserving and passing surface temperatures derived in the surface models into the atmospheric model along with implementing spectral emissivity values in the atmospheric model and updated broadband surface emissivity in surface models (as discussed in section 2.1) improves model performance for prognosing Northern Hemisphere sea ice.

However, in the Southern Hemisphere, there is not a marked improvement between CESM-$\epsilon(\nu)$ and CESM-LME. The austral summer (January, February, March) sea ice decline of -9.1 ± 3.7%/decade and -7.1 ± 1.0%/decade for CESM-$\epsilon(\nu)$ and CESM-LME twentieth century forcing ensemble mean, respectively, are both inconsistent with observed satellite data record sea ice extent growth of $+0.95 \pm 0.23$%/decade from 1979 to 2006 (Comiso & Nishio, 2008). These findings indicate that some combination of poorly modeled cloud radiative effects (Lawson & Gettelman, 2014) and southern ocean dynamics need to be addressed before the impacts of surface emissivity can be properly considered.

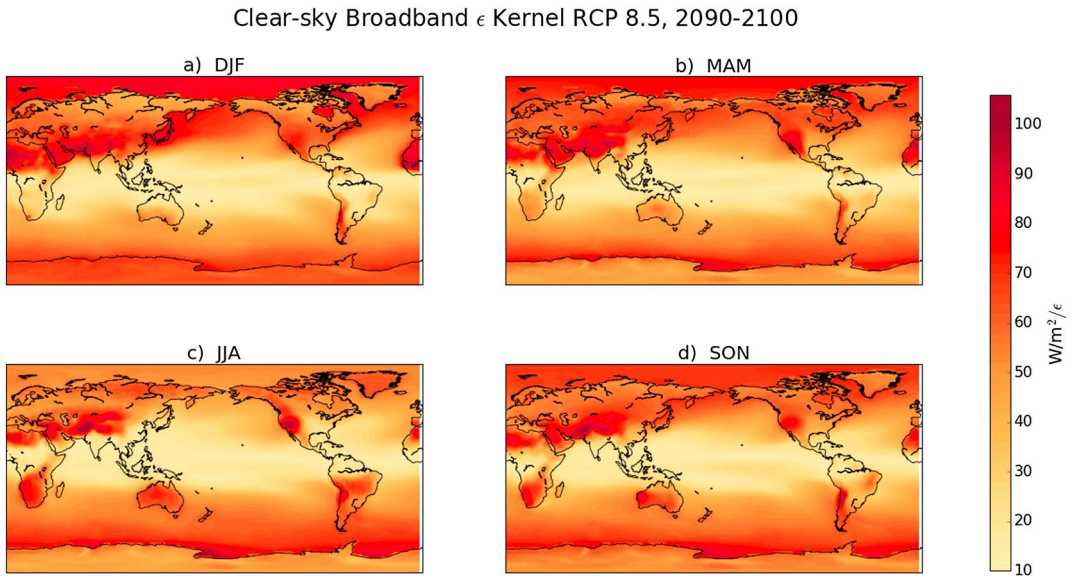

Figure 3. For the RCP8.5 case, end-of-century 10 year averaged clear-sky ϵ kernel maps for four seasons: (a) December-January-February, (b) March-April-May, (c) June-July-August, and (d) September-October-November.

3.2. Emissivity and Kernels

3.2.1. Kernels

Global patterns of emissivity kernels are necessarily positive in sign and are inversely related to maps of column water. Figures 3 and 4 show clear-sky and all-sky seasonal kernel maps, respectively, and reveal that the broadband kernels are strongest at high-altitude regions, dry hot climates, and high latitudes, all of which exhibit low column water vapor (Feldman et al., 2014). Positive trends in water vapor over high-latitude oceans in the summer months induce kernel amplitude suppression and can be seen in seasonal all-sky kernel maps.

3.2.2. Surface Emissivity Evolution

Figure 5 shows the change in surface emissivity for wavenumbers in the atmospheric window (820–980 cm^{-1}, RRTMG_LW band 6) between 1850CNTL and the RCP8.5 runs at the end of the 21st century. These maps show prominent reductions in surface emissivity (blue) at high latitudes in summer and fall seasons in the RCP8.5 run relative to the 1850CNTL run, and these reductions are collocated with increasing sea ice melt. The maps also show increased emissivity (red) in mid- to high-latitude continental regions in winter and spring months,

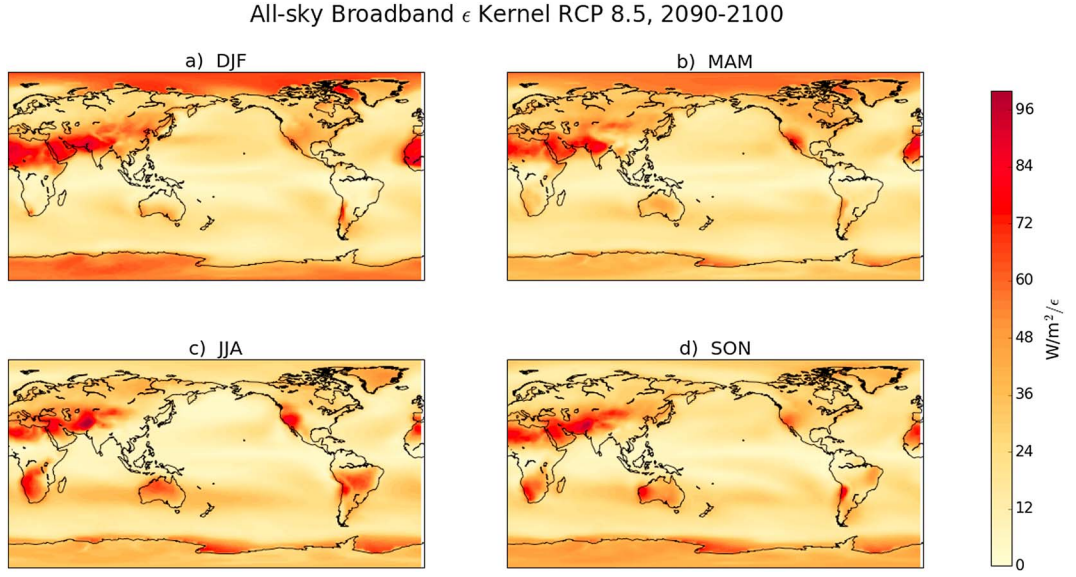

Figure 4. Same description as Figure 3 but for all-sky ϵ.

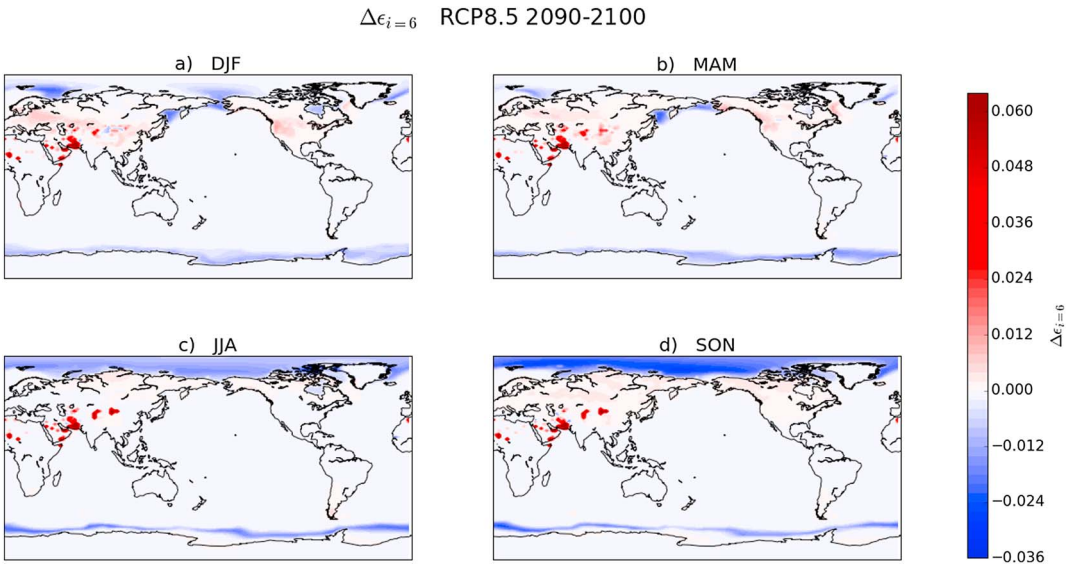

Figure 5. Emissivity difference in RRTMG_LW band 6 between 10 year average in RCP8.5 end of century and a 10 year average of 1850CNTL, for four seasons: (a) December-January-February, (b) March-April-May, (c) June-July-August, and (d) September-October-November. Red regions denote increased emissivity and in blue areas, the emissivity has reduced.

and we can attribute this result to increased greening of dry desert and high-altitude continental regions in RCP8.5 as compared to 1850CNTL.

These maps also show the concurrent effect of sea ice loss and changing atmospheric water vapor and clouds. The summer and fall exhibit the largest emissivity decrease over high-latitude oceans, which reduce emissivity kernel strength (Figures 3 and 4) and thereby outgoing longwave radiation at the top of the model. The inverse spatial correlation of emissivity change and transient kernel strength contributes to moderating the top-of-the-model emissivity feedback.

3.2.3. Spectrally Resolved Emissivity Kernels

Figure 6 shows the spectral variations in surface emissivity kernels and their relative contribution to the broadband kernel, as a function of RRTMG_LW band numbers (Table 1). Figures 6a and 6b show the clear-sky and all-sky globally averaged spectral kernel amplitudes, and the globally averaged spectral emissivity change from 10 years of the 1850CNTL run is shown in Figure 6c for RCP8.5 years 2090–2100. The spectral kernel shape over the RRTMG_LW bands is similar in all four CESM model runs, and the kernel amplitude in band 6 (820–980 cm^{-1}), which corresponds to the mid-infrared atmospheric window, is the dominant contributor. The shape of the spectral emissivity change highlights the differences in spectral emissivity values used for ocean and snow. Except for Band 16 (2,600–3,250 cm^{-1}), where $\epsilon_{\text{water}}(\nu) > \epsilon_{\text{medium-snow}}(\nu)$ for $3,000 < \nu < 3,250\ cm^{-1}$, the emissivity of medium-grained snow exceeds that of ocean. Even though band 6 is the dominant contributor to the kernel, this band shows the smallest difference between ocean and medium-grained snow. Each of the bands 7–9 (encompassing 980–1,390 cm^{-1}) exhibit comparable emissivity radiative response magnitudes to band 6. Snow emissivity values are larger than water emissivity from 980 to 1,390 cm^{-1} for the snow grain sizes measured by Hori et al. (2006). Within band 6, the emissivity of coarse snow grain sizes (800 μm median diameter) is lower than water, and consequently for this band, $\delta\epsilon_{i=6}$ would be positive under sea ice loss.

3.2.4. Kernel Temporal Evolution

The temporal evolution of globally and annually averaged broadband clear-sky emissivity kernels for the four CESM runs are plotted as solid lines in Figure 7a, along with polynomial fits (dotted lines). The all-sky kernels are shown as ratios to clear-sky kernels in the same figure, as dashed lines, and are a little more than 50% of the clear-sky amplitude. Relative to the forced cases, the 1850CNTL kernels are temporally stable. Kernel amplitudes for CO_2-forced atmospheres are not stationary in time nor are they linear, demonstrating that by the end of the 21st century, large biases could be introduced into quantifying feedback by applying the first year's climate base state kernel. For the model specifications of this work, by the end of the 21st century the

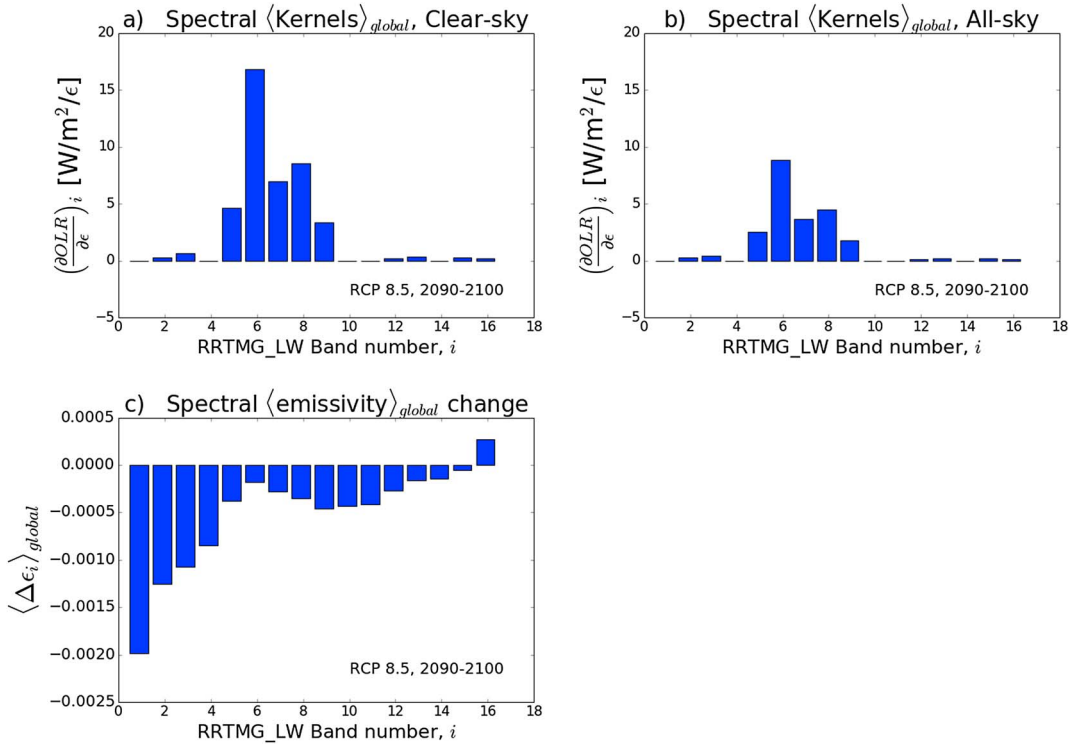

Figure 6. Globally and temporally averaged spectral kernel amplitudes by RRTMG_LW band, for the last 10 years end-of-century RCP8.5 case for (a) clear-sky and b) all-sky. (c) The globally and temporally averaged spectral emissivity change of the last 10 years of RCP8.5 and 10 years of 1850CNTL.

RCP8.5 scenario kernels are reduced by nearly 21% from 1850CNTL and reduced by approximately 17% from the present-day kernel (HISTCO2 at year 2005).

Figure 7b shows the globally and annually averaged climatological surface broadband emissivity change with respect to 1850CNTL for each CESM model run. Absolute values are less than a percent, due to globally averaged values of surface emissivity changes occurring primarily in the cryosphere (which covers about 20% of Earth's surface area), much like surface albedo. In the 1850 control climate, low fluctuations around zero exist for emissivity differences, which we attribute to sea ice melt and freeze. Considering that ocean emissivity is

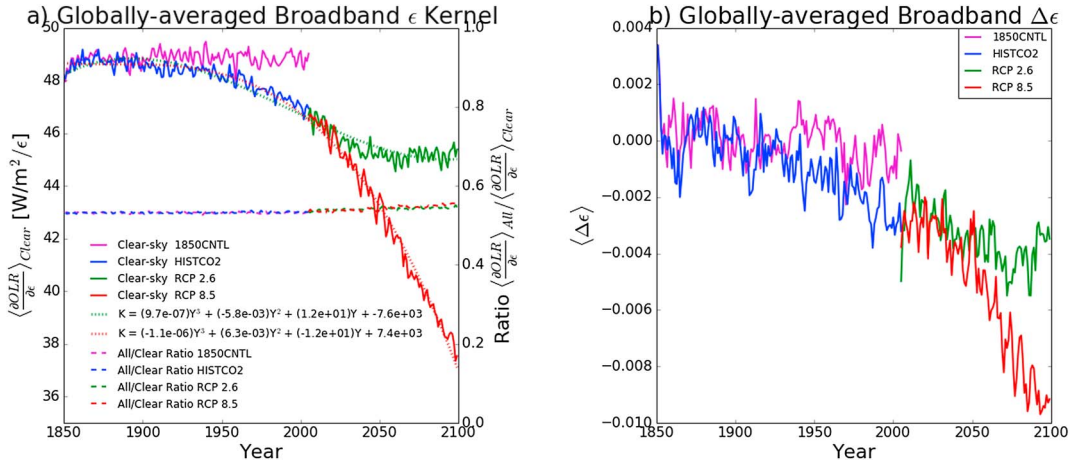

Figure 7. Temporal evolution of emissivity kernels and climatological emissivity change. (a) Solid lines show globally averaged broadband clear-sky ϵ kernel strength in units of W/m^2/ϵ. Dotted lines are polynomial fits to the clear-sky kernels. Dashed lines are ratios of all-sky to clear-sky globally averaged broadband ϵ kernel amplitudes and are unitless. (b) Globally averaged broadband emissivity change with respect to the 1850CNTL case.

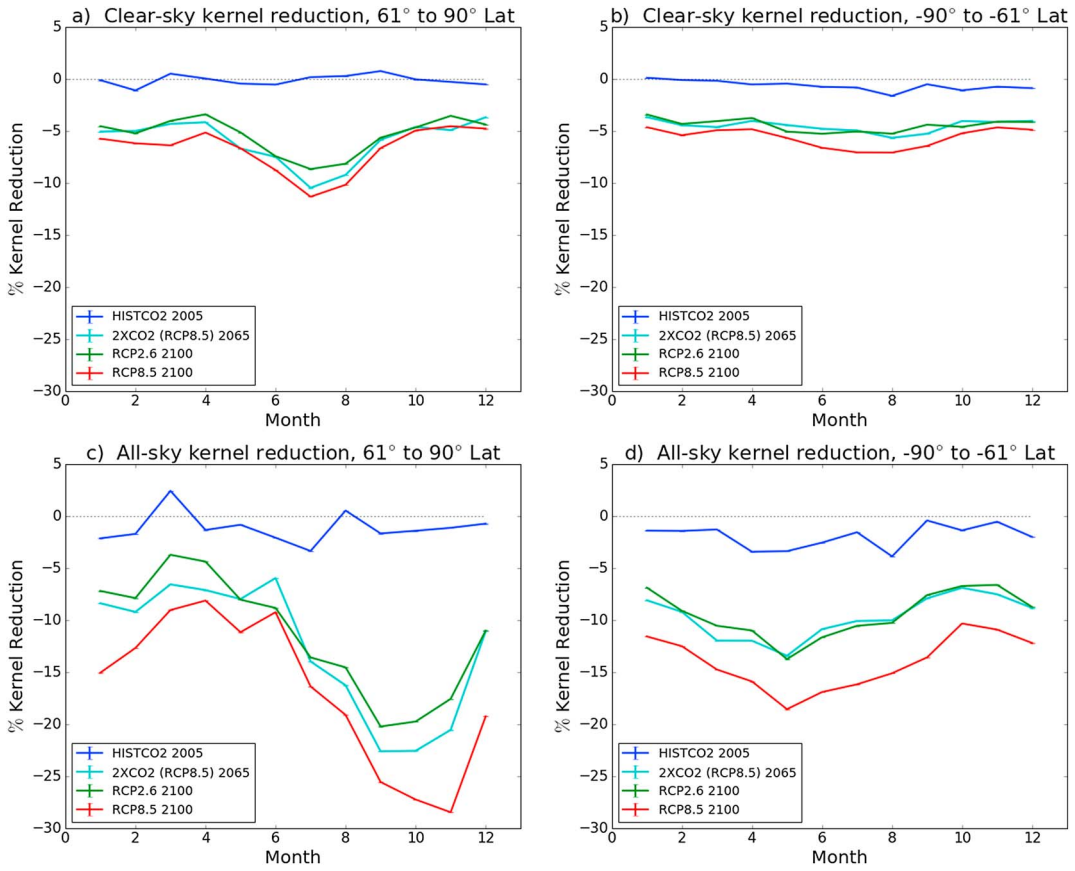

Figure 8. Broadband kernel reduction for forced CO_2 atmosphere cases, with respect to the 1850CNTL case. Clear-sky kernel reductions area-averaged in (a) northern and (b) southern high latitudes. The all-sky cases area-averaged in (c) northern and (d) southern high latitudes.

lower than that of this model's designation of medium-grained snow in the strong kernel RRTMG_LW band 6, negative surface emissivity change of values for all CO_2 forcing cases is the result of a decreased frozen surface extent in the future.

Over the last 10 years of each scenario period, monthly averaged high-latitude broadband kernel reductions relative to 1850CNTL are shown in Figure 8. HISTCO2 monthly kernel amplitude temporal shape over an annual period varies by less than 3% from 1850CNTL; however, monthly kernel amplitudes for RCP2.6 and RCP8.5 can decrease by as much as 10% in clear-sky cases, and almost 30% for all-sky cases in high latitudes. This indicates the problematic nature of implementing radiative kernels calculated from only one year's atmospheric state in the course of analysis of the contribution of the ice emissivity feedbacks over multiple decades. We also note that the seasonal variability in high-latitude kernels is highly asymmetric between the Arctic and the Antarctic. The seasonality that we find in the Arctic under clear-sky conditions is largely a function of the seasonality in atmospheric precipitable water vapor (Figures 9a and 9b). The all-sky seasonality is impacted by enhanced cloud fractional coverage (Figures 9c and 9d) associated with sea ice loss, which has been consistently observed in CMIP3 and CMIP5 models (Karlsson & Svensson, 2013). In the Antarctic, however, the clear-sky kernel reduction is largely invariant through the seasons, except for the end of the century RCP8.5 case, where the southern winter warms.

The monthly evolution of spectral kernels for high latitudes for the last 10 years' of the RCP 8.5 scenario is shown in Figure 10. Figures 10a and 10b show the monthly kernel amplitude for northern high-latitude clear-sky and all-sky conditions, respectively, and are affected by the seasonality in water vapor (Figure 9). The effects of ozone in the southern high latitudes can also be seen in bands 6 and 7, where rising O_3 concentrations in the winter months decrease the kernel strength, and are shown in Figures 10c and 10d for clear- and all-sky conditions, respectively. RRTMG_LW bands 2 and 3, in the water vapor rotational absorption feature shows the most pronounced seasonality due to the seasonality in column water vapor.

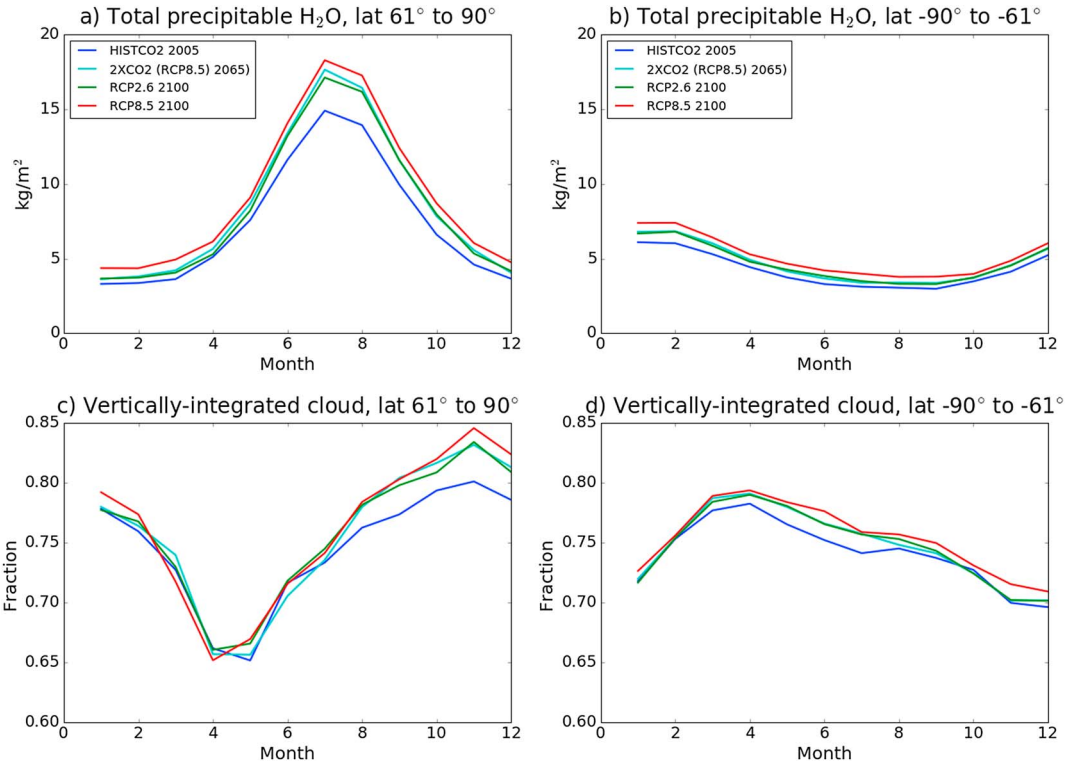

Figure 9. Total precipitable water and total cloud fraction for forced CO_2 atmosphere cases. Area-averaged in (a) northern and (b) southern high latitude total precipitable water. Area-averaged total cloud fraction in (c) northern and (d) southern high latitudes.

The climatological spectral surface emissivity change $\Delta\epsilon_i(t)$ (equation (5)) relative to 1850CNTL is plotted for each month in a 10 year average of years 2090–2100 of RCP8.5 in Figures 11a and 11b, at northern and southern high latitudes, respectively. The climatological surface emissivity change for the end of the century RCP 8.5 scenario is negative for all months and RRTMG_LW bands except springtime high northern latitudes band 16, where ocean emissivity is larger than medium-grained snow emissivity above 3,000 cm^{-1}. The climatological surface emissivity change is largest in the summer and early autumn in high northern latitudes, indicating increased thaw during the typical Arctic melt season. The weak spectral surface emissivity change in the springtime indicates wintertime Arctic sea ice coverage persistence (75% of preindustrial) even at the end of the century in RCP8.5. In the southern high latitudes, the climatological spectral surface emissivity change is the most negative during the winter months, during which climatological surface temperature increase is also largest (60% relative to HISTCTL).

Focusing on the last 10 years of the RCP 8.5 scenario, the average seasonal spectral surface emissivity change, $\delta\epsilon_i(t)$ (equation (6)), a contribution to the surface radiative response from month-to-month is seen in Figures 11c and 11d, again for northern and southern high latitudes, respectively. Cryospheric phase changes can be observed in the seasonal cycle emissivity change between the northern and southern high latitudes, with freezing periods producing positive $\delta\epsilon_i(t)$ and negative $\delta\epsilon(t)$ for melt periods. Atmospheric dynamics effects on phase changes are evident from the structure in Figure 11c, where continental and ocean current spatial distribution in the Arctic impose complexity. In contrast, consistent transitions throughout the bands and months occur in the Antarctic (Figure 11d), where cryospheric changes are more established on sea ice. Note that the $\delta\epsilon_i(t)$ amplitudes determined here are a product of the assigned spectral emissivity values for water and medium-grained snow, which is a simplification for seasonal emissivity values of frozen surfaces. Snow cover on ice sheets will evolve from fine-grained deposition in the cold and windy months to coarse grains as seasonal temperatures rise. While not a focus in this study, the foundation for surface emissivity feedback analysis incorporating seasonal snow grain size-dependent spectral emissivity has been built with this work.

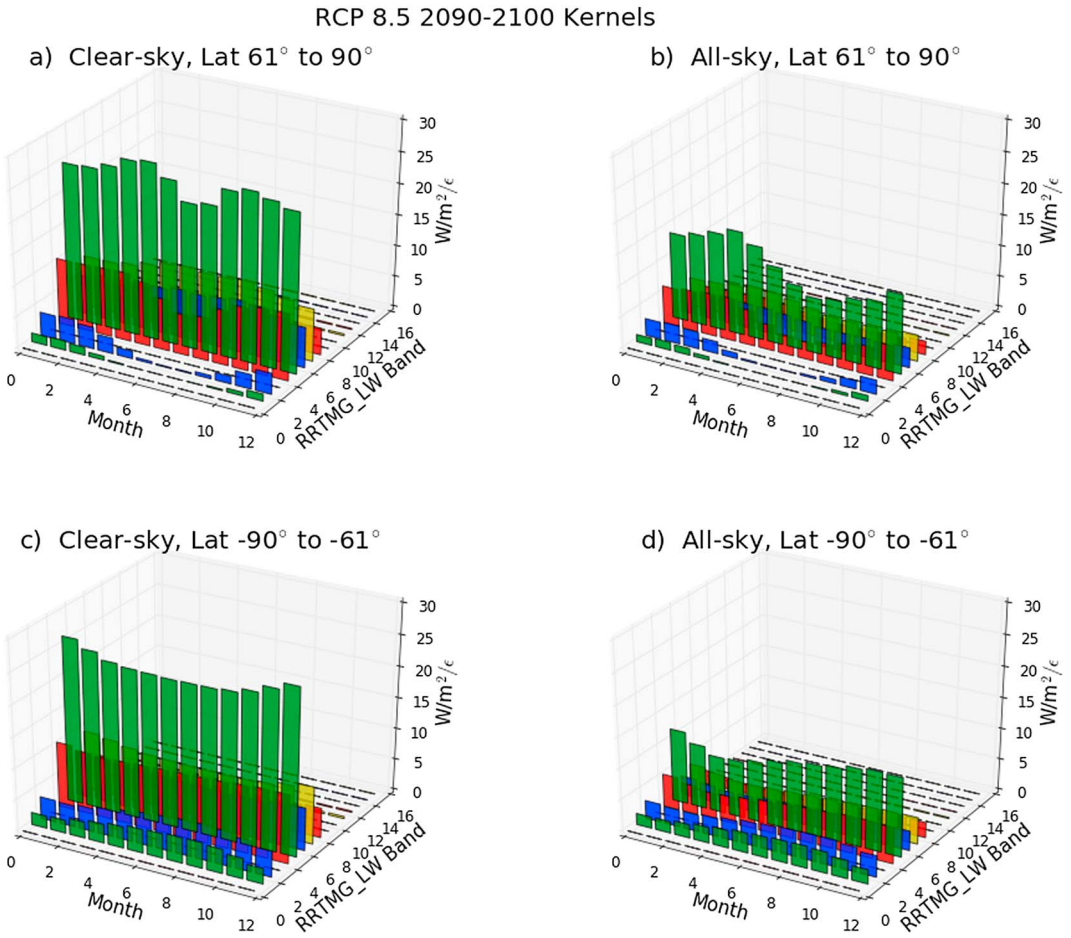

Figure 10. Spectral ϵ kernels for RCP8.5 scenario in high northern latitudes (a) clear-sky and (b) all-sky, and in high southern latitudes (d) clear-sky and (e) all-sky, on a monthly basis. The color scheme for RRTMG_LW bands is [red, green, blue, yellow] for bands = [1,2,3,4] and repeated 3 more times up to band 16.

3.3. Emissivity Feedbacks

3.3.1. Conventional Feedback Analysis

To put the emissivity feedback magnitude into the context of conventional climate feedback analysis, we first report the global emissivity feedback, λ_ϵ, as one component of the total feedback parameter λ, as defined by Wetherald and Manabe (1988). In this form, the emissivity radiative response relative to preindustrial period is normalized by the global mean temperature change. Noting the surface emissivity kernel evolution due, largely, to water vapor dependence, we show the feedback on the 1850CNTL model by calculating surface emissivity kernels from the 1850CNTL, as well as referencing $\Delta\epsilon_i(\vec{r},t)$ with t_0 as the 1850CNTL period.

Zonally and temporally averaged cryosphere emissivity feedbacks are shown in Figure 12 with conventional feedback analysis. The globally averaged surface temperature difference $\Delta\bar{T}_S$ in each scenario was obtained by subtracting a 1850CNTL 10 year averaged monthly global mean surface temperature from monthly surface temperature of each scenario over a 10 year period, ending at the year appearing in the Figure 12 legend. In the four scenarios starting with present day, the climatological emissivity response, $\Delta\epsilon_i(\vec{r},t)$ is determined by differencing ϵ at each spectral band, year, month, and grid cell in these 10 year periods with a 10 year averaged 1850CNTL spectral ϵ for each month and grid cell. Feedback analysis is only considered in a spatiotemporal grid point for which $\Delta\bar{T}_S$ is significant, that is, when $\Delta\bar{T}_S > \sigma_{T_S}$, where σ_{T_S} is the surface temperature standard deviation over the 10 year period for a particular month. Therefore, feedbacks are zonally and temporally averaged by the number of contributing nonzero grid values. Insignificant values of $\Delta\bar{T}_S$ may occur for HISTCO2, but are generally avoided in the future CO_2 forcing scenarios. Grid cells for which CESM history field `ICEFRAC` or `FRACSNO` contained values >0.0 for any monthly averaged time point over the analysis period were considered to be members of the cryosphere. Feedbacks for HISTCO2 are much larger than the forced

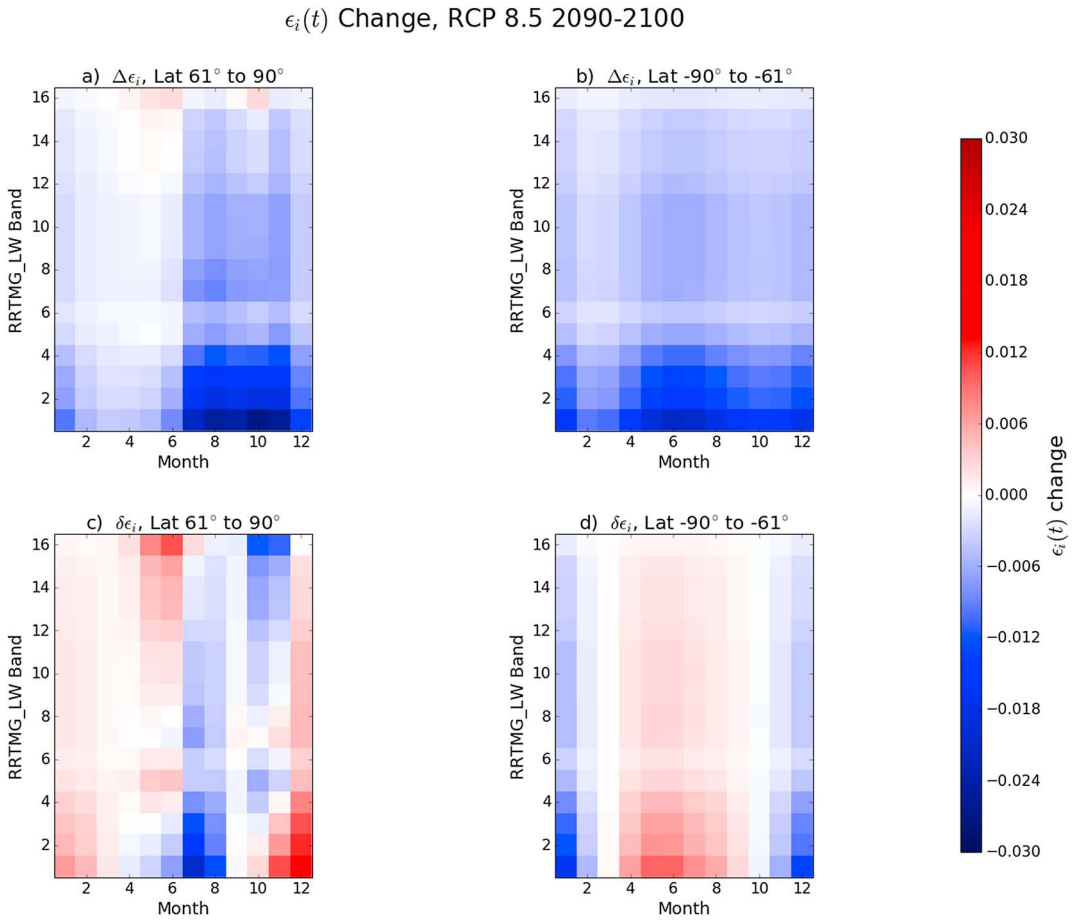

Figure 11. Average spectral climatological surface ϵ change on a monthly basis between 2090–2100 in RCP8.5 scenario and 10 years of 1850CNTL for (a) high northern latitudes and (b) high southern latitudes. Average seasonal month-to-month surface ϵ change in years 2090–2100 of RCP8.5 scenario for (c) high northern latitudes and (d) high southern latitudes. See equations (5) and (6) for $\Delta\epsilon_i$ and $\delta\epsilon_i$ definitions.

runs due to $\Delta\bar{T}_S$ values which are small and somewhat unstable compared to those of future forcing scenarios. Sea ice emissivity global mean feedback amplitude is stable with increasing future CO_2 forcing due to linear kernel strength scaling with rising global mean temperature, and mean zonal broadband $\Delta\epsilon$ amounting to $\mathcal{O}(10^0)$%. However, the spatial distribution of increasing feedback moves poleward, which is consistent with increased sea ice melt at higher latitudes. Our diagnosed ice emissivity feedbacks can then be compared to other well-known feedbacks, such as that due to surface albedo (Armour et al., 2013; Crook & Forster, 2014; Flanner et al., 2011; Hall & Qu, 2006; Winton, 2006). We do note that the all-sky emissivity feedback is dependent on clouds, which will complicate the feedback analysis.

Considering the nonlinearity of the emissivity kernels, we compare feedback calculations based on static kernels $K(t_{\text{ref}})$ (where t_{ref} is the reference time period) against those calculated with time-dependent/dynamic kernels $K(t)$ to look at calculation biases with respect to agreement between methods. For each CO_2 forced case, surface emissivity feedbacks are computed for increasing specification: from global, cryospheric, to sea ice emissivity feedbacks; the latter two separated into Northern and Southern Hemispheres (0° to 90° latitude and −90° to 0° latitude). When comparing different reference periods in static kernel use (Figure 13a), in which both the static kernels and climatological emissivity change differ, the mean bias between surface emissivity feedback calculation methods is 1.16×10^{-3} W/m^2/K. When comparing surface emissivity feedbacks calculated using static kernels against using time-dependent kernels (Figure 13b) for the same reference period, the bias is almost twice as large at 1.95×10^{-3} W/m^2/K. In the use of time-dependent kernels in feedback calculations (Figure 13c), the mean bias between different reference periods is reduced down to

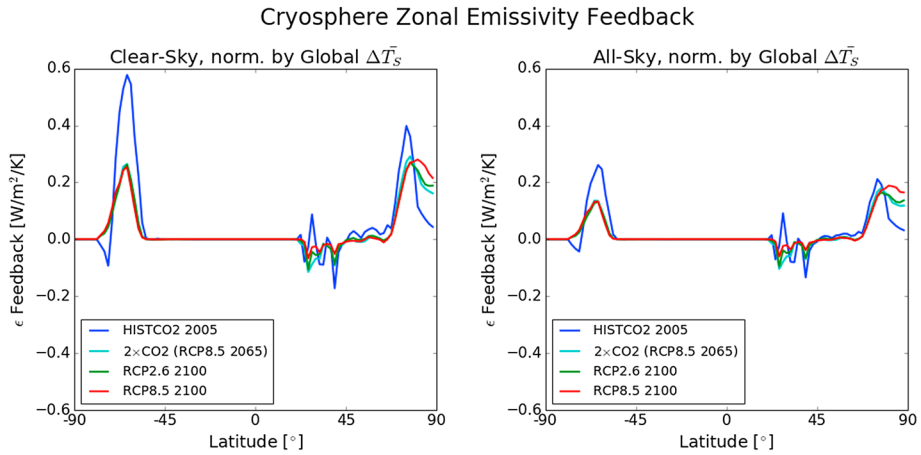

Figure 12. Zonally averaged emissivity feedback of cryosphere for each of the four CO_2 forced cases, relative to 1850CNTL. Kernels from 1850CNTL atmosphere were used in this case, with clear-sky on the left and all-sky on the right plot. Normalization by global mean $\Delta\bar{T}_S$, for conventional prescription of feedback. The HISTCO2 feedback is large due to smaller global mean $\Delta\bar{T}_S$.

8.01×10^{-4} W/m^2/K (compare to Figure 13a). In the previous three cases, surface emissivity feedback was calculated in the conventional method, relative to the global mean surface temperature change.

We must also consider the appropriateness of using global mean surface temperature change for high-latitude feedbacks. While surface albedo feedback studies such as Bony et al. (2006), Sanderson et al. (2010), and Winton (2006) normalized the surface albedo radiative response with respect to global mean surface temperature change, Hall & Qu (2006), Flanner et al. (2011), Colman (2013), Crook & Forster (2014), and Qu and Hall (2014) have implemented regional surface temperature change in their formulation of surface albedo feedback to compare seasonal to climatological surface albedo feedback. By using zonal mean surface temperature change as $\Delta\bar{T}_S$ in equation (3), we find minimal bias (-1.72×10^{-4} W/m^2/K) when using time-dependent kernels, as shown in Figure 13d, where we compare preindustrial and present-day kernel calculations. Indeed, with the smallest bias, Figure 13d shows that the determination of the surface emissivity feedback should be based on the localized surface temperature change rather than the global surface temperature change, in order to provide a more physically mechanistic formulation of this feedback. The biases in Figures 13a–13d are respectively then 43%, 72%, 29%, and 6% of the mean global sea ice emissivity feedback calculated by time-dependent kernels with normalization with zonal mean surface temperature change. The largest bias occurs in the case comparing emissivity feedbacks calculated by static versus time-dependent radiation kernels normalized by climatological global mean temperature differences (Figure 13b), and smallest feedback bias exists when applying time-dependent kernels normalized by mean zonal temperature changes from different reference periods (Figure 13d).

Directing attention to frozen and unfrozen water surfaces, for which theoretical longwave emissivity values were derived by coauthors in Chen et al. (2014) and Huang et al. (2016), we list globally averaged sea ice emissivity feedback values derived from static kernels and time-dependent/dynamic kernels in Table 2. Surface emissivity feedback values are also separated in the table by two methods of surface temperature change: the global mean surface temperature difference and zonal mean surface temperature difference. Static surface emissivity kernels, surface emissivity change, and surface temperature change are referenced to the 1850CNTL atmosphere. Parameter standard deviations over the 10 year periods are propagated into feedback uncertainties expressions for each of the four feedback calculation types. Focusing the discussion to future forcing scenarios, clear-sky sea ice surface emissivity feedbacks determined with dynamic kernels are on the order of 90% of those determined with static kernels, and all-sky dynamic kernel sea ice emissivity feedbacks are less than 60% of static kernel derived values. Normalizing by the zonal mean surface temperature difference, mechanistically more physical, reduces the sea ice surface emissivity feedback values by roughly 50%, compared to normalization by the global mean surface temperature difference. As the most physical method in Table 2, time-dependent kernel feedback calculation with normalization by zonal mean surface temperatures produce clear-sky sea ice emissivity feedback values that are less than 50% of values when calculated with static kernels and with normalization by global mean surface temperature difference. For all-sky,

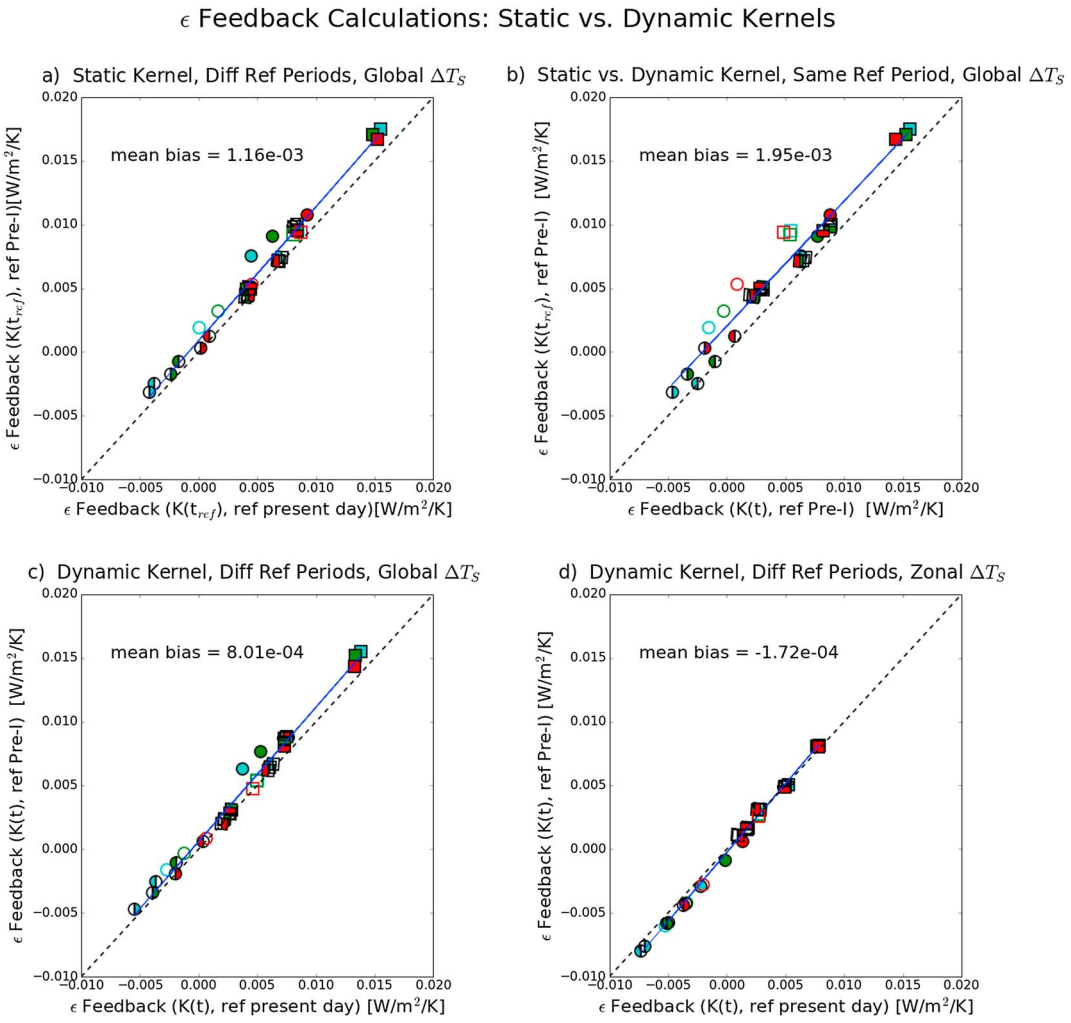

Figure 13. Sea ice emissivity feedbacks calculated using different reference periods and kernel types (static or time dependent/dynamic). (a) Comparison of two different reference periods, each using their respective static kernel. (b) For the same reference period, comparison of feedback using static kernel versus dynamic kernel. (c) Comparison of two different reference periods, each using their respective dynamic kernels. (d) Comparison of two different reference periods, each using their respective dynamic kernels, but feedback is normalized by zonal mean temperature. Marker colors indicate the model case, as described in other figures in this manuscript. Marker fill styles indicate: left fill: clear-sky Northern Hemisphere (NH), right fill: all-sky NH, bottom fill: clear-sky Southern Hemisphere (SH), top fill: all-sky SH, full fill: clear-sky global, no fill: all-sky global. The line of agreement is the black dashed line, and the blue line is a linear regression.

time-dependent kernel, zonal mean surface temperature-derived sea ice emissivity feedback values are less than 30% of static kernel, global mean surface temperature feedback values.

Surface emissivity feedbacks for CO_2 forcing scenarios referenced to 1850CNTL and calculated with their respective time-dependent clear- and all-sky kernels are shown in Figure 14 for Northern and Southern Hemispheric, and global means, for which mean surface temperature change is calculated zonally. Northern Hemisphere cryosphere includes snow-covered land, and as vegetated areas become more exposed in the RCP 21st century CO_2 forcing scenario wintertime, surface emissivity feedbacks are negative for $\epsilon_{veg} > \epsilon_{snow}$, yet increase with forcing strength. The Southern Hemisphere cryosphere surface emissivity feedbacks are due to changes in the distribution of sea ice, as their values are equivalent to the sea ice emissivity feedback; they are exclusively positive, denoting sea ice melt in future scenarios compared to the reference period. Despite undergoing less sea ice melt, Southern Hemisphere cryosphere/sea ice emissivity feedbacks are larger in amplitude than Northern Hemisphere feedbacks due to the larger Southern Hemisphere sea ice surface area. For both hemispheres, the sea ice surface emissivity feedback is stable throughout the forcing scenarios

Table 2
Sea Ice Emissivity Globally Averaged Feedbacks ($W/m^2/K$)

			Kernel	
$\Delta\bar{T}_S$	Sky	Case	Static	Time-dependent/Dynamic
Global mean	Clear	HISTCO2	$3.27 \times 10^{-2} \pm 1.49 \times 10^{0}$	$3.05 \times 10^{-2} \pm 2.29 \times 10^{-3}$
		2×CO_2, RCP8.5 2065	$1.75 \times 10^{-2} \pm 1.28 \times 10^{-3}$	$1.55 \times 10^{-2} \pm 3.46 \times 10^{-4}$
		RCP2.6 2100	$1.71 \times 10^{-2} \pm 1.31 \times 10^{-3}$	$1.52 \times 10^{-2} \pm 3.50 \times 10^{-4}$
		RCP8.5 2100	$1.67 \times 10^{-2} \pm 7.54 \times 10^{-4}$	$1.43 \times 10^{-2} \pm 1.95 \times 10^{-4}$
	All	HISTCO2	$1.50 \times 10^{-2} \pm 1.16 \times 10^{0}$	$8.15 \times 10^{-3} \pm 1.63 \times 10^{-3}$
		2×CO_2, RCP8.5 2065	$9.53 \times 10^{-3} \pm 1.28 \times 10^{-3}$	$5.44 \times 10^{-3} \pm 2.56 \times 10^{-4}$
		RCP2.6 2100	$9.22 \times 10^{-3} \pm 1.32 \times 10^{-3}$	$5.38 \times 10^{-3} \pm 2.53 \times 10^{-4}$
		RCP8.5 2100	$9.46 \times 10^{-3} \pm 7.70 \times 10^{-4}$	$4.79 \times 10^{-3} \pm 1.95 \times 10^{-4}$
Zonal mean	Clear	HISTCO2	$8.49 \times 10^{-3} \pm 2.05 \times 10^{-3}$	$8.06 \times 10^{-3} \pm 1.92 \times 10^{-3}$
		2×CO_2, RCP8.5 2065	$9.19 \times 10^{-3} \pm 3.47 \times 10^{-4}$	$8.19 \times 10^{-3} \pm 2.38 \times 10^{-4}$
		RCP2.6 2100	$9.03 \times 10^{-3} \pm 3.28 \times 10^{-4}$	$8.11 \times 10^{-3} \pm 2.32 \times 10^{-4}$
		RCP8.5 2100	$9.26 \times 10^{-3} \pm 2.40 \times 10^{-4}$	$8.05 \times 10^{-3} \pm 1.47 \times 10^{-4}$
	All	HISTCO2	$3.71 \times 10^{-3} \pm 2.01 \times 10^{-1}$	$2.32 \times 10^{-3} \pm 2.01 \times 10^{-1}$
		2×CO_2, RCP8.5 2065	$4.55 \times 10^{-3} \pm 3.77 \times 10^{-4}$	$2.77 \times 10^{-3} \pm 2.39 \times 10^{-4}$
		RCP2.6 2100	$4.44 \times 10^{-3} \pm 6.99 \times 10^{-4}$	$2.75 \times 10^{-3} \pm 3.92 \times 10^{-4}$
		RCP8.5 2100	$4.82 \times 10^{-3} \pm 2.74 \times 10^{-4}$	$2.62 \times 10^{-3} \pm 1.52 \times 10^{-4}$

Note. See text for further details.

as indicated by feedback calculations for the last 10 years of each scenario period. Driving this stability is that the time-dependent sea ice emissivity radiative response is counterbalanced by zonally averaged surface temperature change (e.g., Figure 13).

3.3.2. Seasonal Response Analysis

Time-dependent emissivity kernels allow us to discern the longwave radiative response of the climate to emissivity changes at time t by examining the emissivity radiative response over the seasonal cycle. Figure 15 plots 10 year averaged emissivity kernels, month-to-month emissivity change ($\delta\epsilon_{i=6}$), and emissivity radiative response for RRTMG_LW band 6 in each column; the top row for sea ice-dominant northern latitudes, and the bottom row for sea ice-dominant southern latitudes. We inspect the atmospheric dynamics, melt/freeze cycle, and emissivity radiative response in these high-latitude regions as they evolve with increased CO_2 forcing.

At high northern latitudes, Figure 15a shows that, due to water vapor, emissivity kernels in wintertime allow more longwave radiation to escape the top of the atmosphere than summertime, for RRTMG_LW band 6. Despite a month-to-month emissivity change ($\delta\epsilon_{i=6}$) with an amplitude larger during melt than freeze periods in future CO_2 forcing scenarios (Figure 15b), the combination of seasonal atmospheric effects on the emissivity kernel and melt/freeze cycle produces a seasonal emissivity radiative response in Figure 15c, which cumulatively over the year is negative in sign (Figure 16). Examination of contributing factors show that the Arctic emissivity kernel amplitude difference between warm and cold seasons becomes larger with increasing CO_2 forcing scenarios, impacting the differential between summertime and wintertime emissivity radiative response. Month-to-month emissivity changes also evolve with increased CO_2 forcing, with an earlier onset springtime melt. However, the wintertime refreeze (February/March) maximum produces a rebound effect that is as large as 84% of preindustrial levels, even at the end of the 21st century. Again, however, the seasonality of the emissivity kernels as shown in Figure 16 stands in contrast to the annually averaged emissivity radiative response.

In the Antarctic, the seasonal emissivity kernel strength (Figure 15d) is influenced by ozone concentration more than water vapor and therefore dips in the southern winter during increased ozone concentration and low water vapor. Thus, the RRTMG_LW band 6 kernels have higher amplitude during the melt season where emissivity changes are negative (Figure 15e). Another feature of note is that for all cases, the southern atmosphere over the sea ice-dominant latitudes does not change significantly from the 1850CNTL atmosphere,

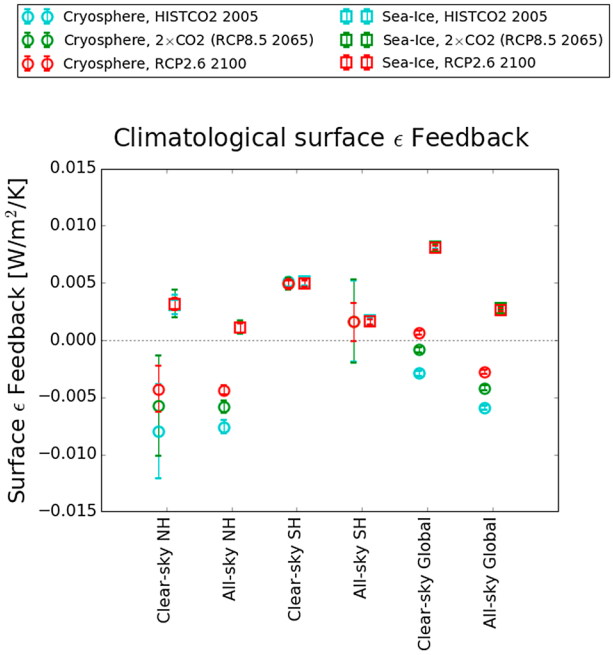

Figure 14. Climatological surface ϵ feedback, calculated with time-dependent kernels of outgoing longwave radiation sensitivity to surface emissivity and zonally averaged surface temperature change, relative to 10 year averages in 1850CNTL. Error bar lengths indicate uncertainties propagated from standard deviations in kernel, surface emissivity, and surface temperature values.

thereby larger amplitude emissivity changes in the future CO_2 forcing scenarios to impose a stronger impact than emissivity kernels in the emissivity radiative response (Figure 15f).

The climatological evolution of seasonal emissivity radiative response (equation (2)) can be seen in Figure 16, where we plot 10 year zonal and annual averages of the seasonal emissivity response (annual average of plots such as Figures 15c and 15f for each latitude). The emissivity radiative response at high northern latitudes shows increasing outgoing radiation with CO_2 forcing, given the seasonal atmospheric dynamics and surface emissivity change oscillation between positive and negative sign. In the southern ocean, the emissivity radiative response in future CO_2 forcing scenarios reduces, signifying positive climatological seasonal emissivity radiative response, given climatologically stable atmospheric dynamics over the southern ocean and modeled climatological decrease in frozen surfaces. Bear in mind that Antarctic sea ice decline is simulated in the CESM models to be much faster than observations, as discussed in section 3.1.1.

Even though we do not make direct comparisons of seasonal with climatological emissivity feedback here, we note the relative sign of the emissivity radiative responses between the periods. The climatological sea ice emissivity radiative response (use of equation (5) in equation (2)) is positive, given the climatological decrease in summertime frozen surfaces and emissivity values for frozen and nonfrozen surfaces specified in this work. However, on short time scales, the seasonal sea ice emissivity radiative response (equation (6) in equation (2)), is about an order of magnitude less than the climatological emissivity radiative response and is consistently negative. Focusing on northern high latitudes, the climatologically accumulated seasonal sea ice emissivity radiative response remains negative. The northern high latitude emissivity radiative response is influenced by two components: first is the declining sea ice and second, the climatologically evolving seasonal emissivity radiative kernels modulate the strength of the emissivity reduction during springtime/summertime

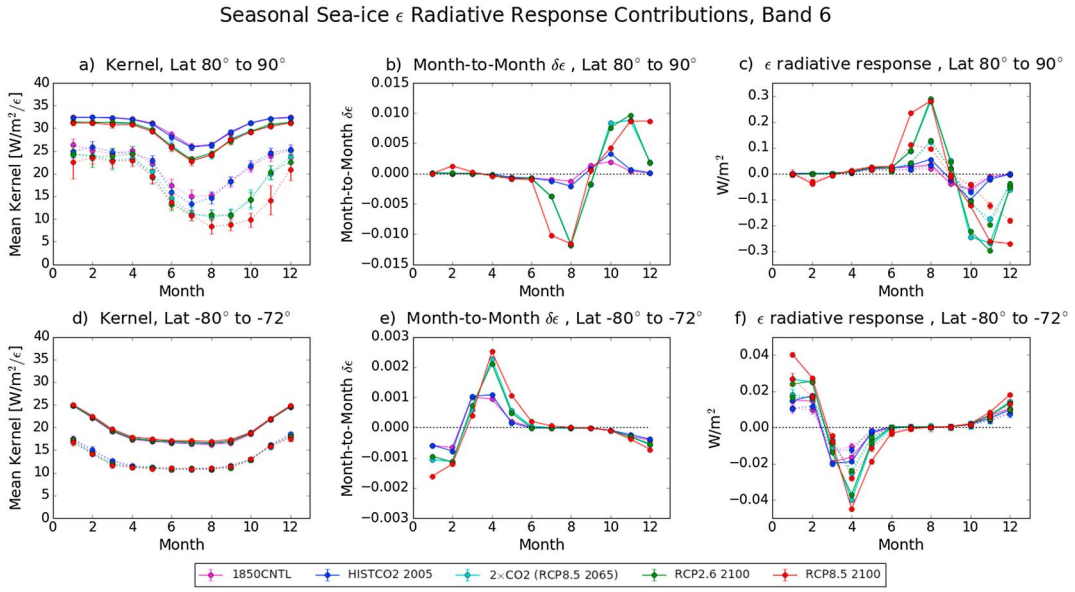

Figure 15. RRTMG_LW band 6 seasonal emissivity radiative response factors for high sea ice-dominant latitudes. (a) northern and (d) southern high-latitude monthly emissivity kernels for the last 10 years of each case, the last year noted in the figure legend. (b) Northern and (e) southern high-latitude month-to-month emissivity change ($\delta\epsilon_{i=6}$, equation (6)). (c) northern and (f) southern high-latitude emissivity radiative response. Error bars are calculated from the 10 year variability. Kernel and radiative response plots use solid lines for clear-sky and dashed lines for all-sky.

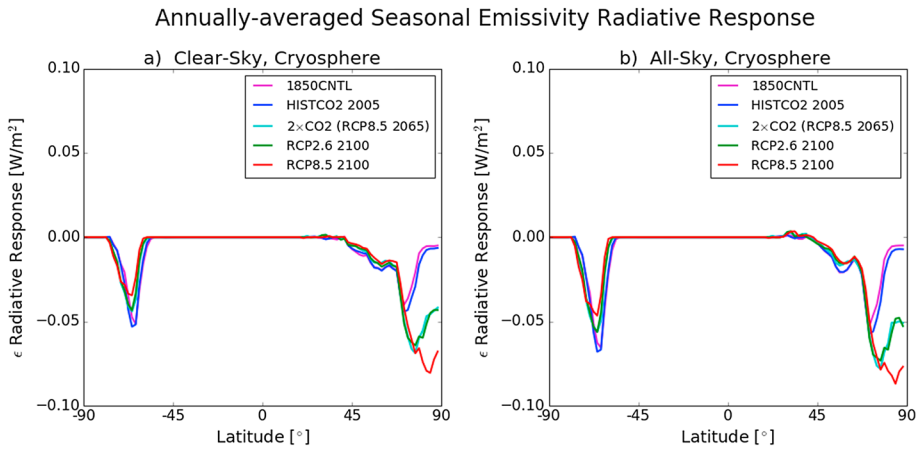

Figure 16. Zonally and time-averaged seasonal emissivity radiative response for each case, using (a) clear-sky kernels, and (b) all-sky kernels. The time average is over 10 year periods ending in the year denoted in the figure legend for each case.

melt, as shown in Figure 15a. In the southern high latitudes over sea ice, the climatological emissivity radiative response is driven by predominantly the surface emissivity differences due to declining sea ice, as water vapor has less seasonal impact on the emissivity radiative kernel than in the northern atmosphere, and therefore the southern high latitude climatological emissivity radiative response is positive.

4. Discussion and Conclusions

We have investigated how the inclusion of realistic and consistent surface emissivity in both land surface and atmospheric components of the CESM coupled-climate model affects a wide range of climate variables. We did this by replacing the broadband emissivity values in RRTMG_LW for water, medium-grained snow, and desert scenes. We find that this harmonized treatment of surface emissivity within CESM can be important for reducing high-latitude temperature biases. We also find that short-term effects of atmospheric dynamics and spectral information need to be considered to understand radiative effects in higher detail and are possible with radiative kernels computed for every grid and time point for the entire model integration period.

We performed feedback analysis and found that sea ice emissivity feedback is positive in sign, which is driven by the differences in emissivity between frozen and unfrozen surfaces at wavenumbers less than 3,000 cm^{-1}. From this single mean state realization represented by our transient model, we have quantified the global sea ice emissivity feedback in an atmosphere at year 2100 in the RCP 8.5 scenario as $+8.05 \pm 0.15 \times 10^{-3}$ $W/m^2/K$ for clear-sky and $+2.62 \pm 0.15 \times 10^{-3}$ $W/m^2/K$ for all-sky, with uncertainties derived from propagation of equation (3) variables' 1 σ deviations over the analysis time period. The global clear-sky sea ice emissivity feedback is a few percent of surface albedo feedback, and this relative amplitude is not unexpected, given that albedo change (tens of percent) is much larger than emissivity change (a few percent), between snow and water. This feedback analysis used spectrally resolved kernels and revealed time-varying interactions between the bands. We can extend this analysis to diagnose the ice emissivity feedback in other Earth system models with off-line calculations of spectral surface emissivity radiative kernels and spectral surface emissivity change for models with sea ice fraction output.

We also note that conventional climatological feedback calculations indicate that this sea ice emissivity feedback is positive in sign but that the radiative effects of the difference in emissivity between frozen and unfrozen surfaces exhibit seasonal dependence. Furthermore, this seasonality itself exhibits meridional asymmetry due to differences in sea ice response to climate forcing between the Arctic and the Antarctic. In the Arctic, this seasonal, temporally higher-order analysis exhibits increasing outgoing surface emissivity radiative response in a warming climate. While the sea ice emissivity feedback and seasonal sea ice emissivity radiative response amplitudes are a few percent of surface albedo feedbacks, the feedback analysis methods outlined in this work demonstrate that spatially and temporally localized feedback analysis can give insight into the mechanisms at work on those scales which differ in amplitude and sign from conventional climatological analyses. This is demonstrated in section 3.3.2, where by executing seasonal surface emissivity response analysis with time-dependent kernels and time-dependent surface emissivity change, the northern

high-latitude climatological surface emissivity radiative response is negative while southern high-latitude climatological surface emissivity radiative response is positive. In the presence of sea ice decline, the Arctic atmospheric dynamics develops in such a way that the climatological surface emissivity radiative response is negative, whereas the Antarctic atmospheric dynamics is rather static over the climatological forcing periods, giving way to positive climatological surface emissivity radiative response. Additionally, the sign between high-latitude climatological surface emissivity radiative response analysis and conventional emissivity feedback analysis can differ if the latter case does not capture underlying driving feedback mechanisms present in a higher-order domain.

The inclusion of this realistic physics leads to improved agreement between CESM model results and Arctic surface temperatures and sea ice trends. This reduction of persistent surface temperature biases suggests that modeling surface emissivity may be a contributing factor to cold-pole model biases, where radiative surface temperatures are constantly being rederived low in RRTMG_LW compared to surface components, when surface emissivity is set to 1.0 in the atmospheric component. To clarify, the CESM1 release version calculates two distinct representations of the surface temperature: the surface temperature derived from subsurface temperature profile models residing in surface model components, and the surface temperature calculated by the Stefan-Boltzmann law with surface emissivity set equal to 1.0. We tried to reconcile the disparate representation of surface temperature to ultimately harmonize the treatment of surface temperature and radiative fluxes. With spectral surface emissivity modeling as outlined in section 2.2, more realistic calculated longwave upward and downward fluxes impact energy balance and surface temperature derivations in the surface components in the next time step. Twenty-four atmospheric GCMs that participated in the CMIP5 (Taylor et al., 2012) assume constant surface emissivity over the entire longwave spectrum, and so the modifications to CESM1 presented here may be relevant for those models.

There is still work to be done regarding ice emissivity feedback analysis, however. First, in these simulations the downward longwave radiative flux still remains decoupled from the ocean model, though we should note that the influence of this decoupling on the results presented here is likely to be small because the longwave extinction coefficient amplitude excludes longwave radiation from transmission beyond the first ocean layer (W. Large, National Center for Atmospheric Research, personal communication, 2017; Smith et al., 2010). Second, the treatment of spectral surface emissivity for vegetated surfaces is incomplete in that its variation based on plant species and far-infrared emissivity for any vegetated scenes is unknown. Third, the dependence of the ice emissivity feedback on snow grain size needs to be explored. We used the spectral emissivity curve for medium-grained snow, but several studies have noted a decrease in emissivity with snow grain size that is spectrally variable (Hori et al., 2006; Huang et al., 2016). Therefore, the sign of the seasonal surface emissivity radiative response and the climatological surface emissivity feedback could depend on the details of snow metamorphosis, which further motivates the need for realistic modeling of snow grain size evolution both in the sea ice and land components of coupled-climate models. Finally, a similar analysis to what is presented here for CESM will need to be performed in other climate models to establish if surface emissivity physics are important for high-latitude feedbacks and bias reduction in the multimodel ensemble.

Acknowledgments
We would like to extend our gratitude to Gautam Bisht, William Riley, Marika Holland, Stephen Yeager, and Elizabeth Hunke for their helpful input, and the anonymous reviewers for their careful evaluation of this work. This material is based upon work supported by the U.S. Department of Energy, Office of Science, Office of Biological and Environmental Research, Scientific Discovery through Advanced Computing, under contract DE-AC02-05CH11231. The authors used resources of the National Energy Research Scientific Computing Center (NERSC), a DOE Office of Science User Facility supported by the Office of Science of the U.S. Department of Energy under that same award. Model output data can be found at http://portal.nersc.gov/project/m2250/emissfdbk/.

References

Arctic Climate Impact Assessment (2005). Arctic climate impact assessment (*ACIA Overview Report*) (p. 1020). New York, NY: Cambridge University Press. ISBN 0 521 86509 3.

Armour, K. C., Bitz, C. M., & Roe, G. H. (2013). Time-varying climate sensitivity from regional feedbacks. *Journal of Climate*, *26*(13), 4518–4534.

Baldridge, A. M., Hook, S. J., Grove, C. I., & Rivera, G. (2009). The ASTER spectral library version 2.0. *Remote Sensing of Environment*, *113*(4), 711–715.

Barton, N. P., Klein, S. A., & Boyle, J. S. (2014). On the contribution of longwave radiation to global climate model biases in Arctic lower tropospheric stability. *Journal of Climate*, *27*(19), 7250–7269.

Bony, S., Colman, R., Kattsov, V. M., Allan, R. P., Bretherton, C. S., Dufresne, J. L., … Randall, D. A. (2006). How well do we understand and evaluate climate change feedback processes? *Journal of Climate*, *19*(15), 3445–3482.

Chen, X., Huang, X., & Flanner, M. G. (2014). Sensitivity of modeled far-IR radiation budgets in polar continents to treatments of snow surface and ice cloud radiative properties. *Geophysical Research Letters*, *41*, 6530–6537. https://doi.org/10.1002/2014GL061216

Colman, R. A., & McAvaney, B. J. (1997). A study of general circulation model climate feedbacks determined from perturbed sea surface temperature experiments. *Journal of Geophysical Research*, *102*(D16), 19383–19402.

Colman, R. A. (2013). Surface albedo feedbacks from climate variability and change. *Journal of Geophysical Research: Atmospheres*, *118*, 2827–2834. https://doi.org/10.1002/jgrd.50230

Comiso, J. C., & Nishio, F. (2008). Trends in the sea ice cover using enhanced and compatible AMSR-E, SSM/I, and SMMR data. *Journal of Geophysical Research*, *113*, C02S07. https://doi.org10.1029/2007JC004257

Crook, J. A., & Forster, P. M. (2014). Comparison of surface albedo feedback in climate models and observations. *Geophysical Research Letters*, *41*, 1717–1723. https://doi.org10.1002/2014GL059280

Dee, D. P., Uppala, S. M., Simmons, A. J., Berrisford, P., Poli, P., Kobayashi, S., … Bechtold, P. (2011). The ERA-Interim reanalysis: Configuration and performance of the data assimilation system. *Quarterly Journal of the Royal Meteorological Society*, *137*(656), 553–597.

English, J. M., Kay, J. E., Gettelman, A., Liu, X., Wang, Y., Zhang, Y., & Chepfer, H. (2014). Contributions of clouds, surface albedos, and mixed-phase ice nucleation schemes to Arctic radiation biases in CAM5. *Journal of Climate*, *27*(13), 5174–5197.

Feldman, D. R., Collins, W. D., Pincus, R., Huang, X., & Chen, X. (2014). Far-infrared surface emissivity and climate. *Proceedings of the National Academy of Sciences*, *111*(46), 16,297–16,302.

Flanner, M. G., Shell, K. M., Barlage, M., Perovich, D. K., & Tschudi, M. A. (2011). Radiative forcing and albedo feedback from the Northern Hemisphere cryosphere between 1979 and 2008. *Nature Geoscience*, *4*(3), 151–155.

Flato, G., Marotzke, J., Abiodun, B., Braconnot, P., Chou, S. C., Collins, W. J., … Forest, C. (2013). Evaluation of climate models. In: Climate change 2013: The physical science basis. Contribution of Working Group I to the Fifth Assessment Report of the Intergovernmental Panel on Climate Change. *Climate Change 2013*, *5*, 741–866.

Gettelman, A., Liu, X., Ghan, S. J., Morrison, H., Park, S., Conley, A. J., … Li, J. L. (2010). Global simulations of ice nucleation and ice supersaturation with an improved cloud scheme in the Community Atmosphere Model. *Journal of Geophysical Research*, *115*, D18216. https://doi.org10.1029/2009JD013797

Hale, G. M., & Querry, M. R. (1973). Optical constants of water in the 200-nm to 200-µm wavelength region. *Applied optics*, *12*(3), 555–563.

Hall, A., & Qu, X. (2006). Using the current seasonal cycle to constrain snow albedo feedback in future climate change. *Geophysical Research Letters*, *33*, L03502. https://doi.org10.1029/2005GL025127

Hansen, J., Nazarenko, L., Ruedy, R., Sato, M., Willis, J., Del Genio, A., … Novakov, T. (2005). Earth's energy imbalance: Confirmation and implications. *Science*, *308*(5727), 1431–1435. https://doi.org10.1126/science.1110252

Hori, M., Aoki, T., Tanikawa, T., Motoyoshi, H., Hachikubo, A., Sugiura, K., & Takahashi, F. (2006). In-situ measured spectral directional emissivity of snow and ice in the 8–14 µm atmospheric window. *Remote Sensing of Environment*, *100*(4), 486–502.

Huang, X., Chen, X., Zhou, D. K., & Liu, X. (2016). An observationally based global band-by-band surface emissivity dataset for climate and weather simulations. *Journal of the Atmospheric Sciences*, *73*(9), 3541–3555.

Hurrell, J. W., Holland, M. M., Gent, P. R., Ghan, S., Kay, J. E., Kushner, P. J., … Lipscomb, W. H. (2013). The Community Earth System Model: A framework for collaborative research. *Bulletin of the American Meteorological Society*, *94*(9), 1339–1360.

Iacono, M. J., Mlawer, E. J., Clough, S. A., & Morcrette, J. J. (2000). Impact of an improved longwave radiation model, RRTM, on the energy budget and thermodynamic properties of the NCAR community climate model, CCM3. *Journal of Geophysical Research*, *105*(D11), 14,873–14,890.

Jackson, C. S., Sen, M. K., Huerta, G., Deng, Y., & Bowman, K. P. (2008). Error reduction and convergence in climate prediction. *Journal of Climate*, *21*(24), 6698–6709.

Karlsson, J., & Svensson, G. (2013). Consequences of poor representation of Arctic sea-ice albedo and cloud-radiation interactions in the CMIP5 model ensemble. *Geophysical Research Letters*, *40*, 4374–4379. https://doi.org10.1002/grl.50768

Kay, J. E., Hillman, B. R., Klein, S. A., Zhang, Y., Medeiros, B., Pincus, R., … Ackerman, T. P. (2012). Exposing global cloud biases in the Community Atmosphere Model (CAM) using satellite observations and their corresponding instrument simulators. *Journal of Climate*, *25*(15), 5190–5207.

Kay, J. E., Deser, C., Phillips, A., Mai, A., Hannay, C., Strand, G., … Holland, M. (2015). The Community Earth System Model (CESM) large ensemble project: A community resource for studying climate change in the presence of internal climate variability. *Bulletin of the American Meteorological Society*, *96*(8), 1333–1349.

Lawson, R. P., & Gettelman, A. (2014). Impact of Antarctic mixed-phase clouds on climate. *Proceedings of the National Academy of Sciences*, *111*(51), 18,156–18,161.

Li, J. (2000). Gaussian quadrature and its application to infrared radiation. *Journal of the Atmospheric Sciences*, *57*(5), 753–765. https://doi.org10.1175/1520-0469(2000)057<0753:GQAIAT>2.0.CO;2

Massom, R. A., Eicken, H., Hass, C., Jeffries, M. O., Drinkwater, M. R., Sturm, M., … Morris, K. (2001). Snow on Antarctic sea ice. *Reviews of Geophysics*, *39*(3), 413–445.

Mauritsen, T., Stevens, B., Roeckner, E., Crueger, T., Esch, M., Giorgetta, M., & Mikolajewicz, U. (2012). Tuning the climate of a global model. *Journal of Advances in Modeling Earth Systems*, *4*, M00A01. https://doi.org/10.1029/2012MS000154

Meehl, G. A., Covey, C., Taylor, K. E., Delworth, T., Stouffer, R. J., Latif, M., … Mitchell, J. F. (2007). The WCRP CMIP3 multimodel dataset: A new era in climate change research. *Bulletin of the American Meteorological Society*, *88*(9), 1383–1394.

Mishchenko, M. I. (1994). Asymmetry parameters of the phase function for densely packed scattering grains. *Journal of Quantitative Spectroscopy and Radiative Transfer*, *52*(1), 95–110.

Mlawer, E. J., Taubman, S. J., Brown, P. D., Iacono, M. J., & Clough, S. A. (1997). Radiative transfer for inhomogeneous atmospheres: RRTM, a validated correlated-k model for the longwave. *Journal of Geophysical Research*, *102*(D14), 16,663–16,682.

Neftel, A., Friedli, H., Moor, E., Lötscher, H., Oeschger, H., Siegenthaler, U., & Stauffer, B. (1994). Historical CO_2 record from the Siple Station ice core, *Trends: A compendium of data on global change. Carbon dioxide information analysis center*. Oak Ridge, TN: Oak Ridge National Laboratory, U.S. Department of Energy.

NOAA ESRL Global Monitoring Division (2015). Updated annually. Atmospheric carbon dioxide dry air mole fractions from quasi-continuous measurements at Mauna Loa, Hawaii. Compiled by K.W. Thoning, D.R. Kitzis, and A. Crotwell. National Oceanic and Atmospheric Administration (NOAA), Earth System Research Laboratory (ESRL), Global Monitoring Division (GMD), Boulder, CO. Version 2015-12 at https://doi.org/10.7289/V54X55RG

Otto-Bliesner, B. L., Brady, E. C., Fasullo, J., Jahn, A., Landrum, L., Stevenson, S., … Strand, G. (2016). Climate variability and change since 850 CE: An ensemble approach with the Community Earth System Model. *Bulletin of the American Meteorological Society*, *97*(5), 735–754. https://doi.org/10.1175/BAMS-D-14-00233.1

Park, T. W., Deng, Y., Cai, M., Jeong, J. H., & Zhou, R. (2014). A dissection of the surface temperature biases in the Community Earth System Model. *Climate dynamics*, *43*(7-8), 2043–2059.

Qu, X., & Hall, A. (2006). Assessing snow albedo feedback in simulated climate change. *Journal of Climate*, *19*(11), 2617–2630.

Qu, X., & Hall, A. (2007). What controls the strength of snow-albedo feedback? *Journal of Climate*, *20*(15), 3971–3981.

Qu, X., & Hall, A. (2014). On the persistent spread in snow-albedo feedback. *Climate Dynamics*, *42*(1-2), 69–81.

Sanderson, B. M., Shell, K. M., & Ingram, W. (2010). Climate feedbacks determined using radiative kernels in a multi-thousand member ensemble of AOGCMs. *Climate Dynamics*, *35*(7), 1219–1236.

Shell, K. M., Kiehl, J. T., & hields, C. A. (2008). Using the radiative kernel technique to calculate climate feedbacks in NCAR's Community Atmospheric Model. *Journal of Climate*, *21*(10), 2269–2282.

Smith, R., Jones, P., Briegleb, B., Bryan, F., Danabasoglu, G., Dennis, J., … Hecht, M. (2010). The Parallel Ocean Program (POP) reference manual ocean component of the Community Climate System Model (CCSM) and Community Earth System Model (CESM) (*Rep. LAUR-01853, 141*). Boulder, CO: University Corporation for Atmospheric Research.

Soden, B. J., Held, I. M., Colman, R., Shell, K. M., Kiehl, J. T., & Shields, C. A. (2008). Quantifying climate feedbacks using radiative kernels. *Journal of Climate*, *21*(14), 3504–3520.

Stroeve, J., Holland, M. M., Meier, W., Scambos, T., & Serreze, M. (2007). Arctic sea ice decline: Faster than forecast. *Geophysical Research Letters*, *34*, L09501. https://doi.org/10.1029/2007GL029703

Taylor, K. E., Stouffer, R. J., & Meehl, G. A. (2012). An overview of CMIP5 and the experiment design. *Bulletin of the American Meteorological Society*, *93*(4), 485–498.

Trenberth, K. E., Fasullo, J. T., & Kiehl, J. (2009). Earth's global energy budget. *Bulletin of the American Meteorological Society*, *90*(3), 311–323. https://doi.org/10.1175/2008bams2634.1

Warren, S. G., Rigor, I. G., Untersteiner, N., Radionov, V. F., Bryazgin, N. N., Aleksandrov, Y. I., & Colony, R. (1999). Snow depth on Arctic sea ice. *Journal of Climate*, *12*(6), 1814–1829.

Warren, S. G., & Brandt, R. E. (2008). Optical constants of ice from the ultraviolet to the microwave: A revised compilation. *Journal of Geophysical Research*, *113*, D14220. https://doi.org/10.1029/2007JD009744

Webster, M. A., Rigor, I. G., Nghiem, S. V., Kurtz, N. T., Farrell, S. L., Perovich, D. K., & Sturm, M. (2014). Interdecadal changes in snow depth on Arctic sea ice. *Journal of Geophysical Research: Oceans*, *119*, 5395–5406. https://doi.org/10.1002/2014JC009985

Wetherald, R. T., & Manabe, S. (1988). Cloud feedback processes in a general circulation model. *Journal of the Atmospheric Sciences*, *45*(8), 1397–1416.

Winton, M. (2006). Surface albedo feedback estimates for the AR4 climate models. *Journal of Climate*, *19*(3), 359–365.